Journal of Engineering Mathematics manuscript No.
(will be inserted by the editor)

Rayleigh-Taylor Instabilities in Miscible fluids with Initially Piecewise Linear Density Profiles

S. Cowell, J. Kent, and P. M. J. Trevelyan

Received: date / Accepted: date

Abstract The stability of some simple density profiles in a vertically orientated two-dimensional porous medium are considered. The quasi-steady state approximation is made so that the stability of the system can be approximated. As the profiles diffuse in time, the instantaneous growth rates evolve in time. For an initial step function density profile, the instantaneous growth rate was numerically found to decay like $T^{-1/2}$ for large times T, so the corresponding eigenfunctions and length of the fingers are expected to scale with $e^{\omega\sqrt{T}}$ where ω is a constant. For density profiles initially corresponding to a finite layer, the instantaneous growth rate eventually decayed like T^{-1}. This corresponds to an instability with algebraic growth, so the eigenfunctions and length of the fingers are expected to scale with T^p (where p is a constant) for large time. For a species initially linearly distributed in a finite layer, when the concentration has an increasing gradient in the downwards direction, the stability of the system was similar to that found for a uniformly distributed finite layer. However, when the concentration had a decreasing gradient in the downwards direction, the growth rates remained constant for a long period time, but eventually decayed in the same way as found in a uniformly distributed finite layer, for very large times. Numerical simulations were performed to validate the predictions made by the linear stability analysis.

Keywords Buoyancy · linear stability · porous media · Darcy's law · nonlinear simulations · piecewise linear profiles

PACS 47.20.Bp · 47.56.+r · 47.11.j

Division of Mathematics & Statistics, University of South Wales, Pontypridd, CF37 1DL, Wales, UK. E-mail: Philip.Trevelyan@southwales.ac.uk

1 Introduction

When a more dense fluid overlies a less dense miscible fluid the resulting instability is named a Rayleigh-Taylor instability [1,2]. This situation can arise in a large number of physical problems, for example within stars [3], the atmosphere [4], the oceans [5] and even beneath the Earth's crust [6]. A useful overview of the Rayleigh-Taylor instability was made by Sharp [7].

Examining the one-dimensional vertical density profile is very useful in determining whether a Rayleigh-Taylor instability will occur, for example, see Citri et al. [8] who analysed density profiles to try to predict whether an instability would occur in reaction-diffusion systems. In finite domains in the presence of linear density profiles the onset condition for a Rayleigh-Taylor instability was first obtained by [9,10]. However, non-monotonic density profiles do not guarantee an instability as, for example, layer thicknesses, viscosity, permeability and diffusion can all affect whether an instability occurs or not. Additionally, having a monotonic density profile does not guarantee the system is stable as other types of instabilities exist, for example salt fingering in oceanography is a double diffusive instability [11–13], that can occur when a less dense faster diffusing species overlies a more dense slower diffusing species. In an infinite vertical domain with an evolving step function density profile, the onset conditions for a buoyancy instability in a porous medium were obtained by [14] by making use of the quasi steady state approximation, so that the base state profiles were assumed frozen in time.

An instability with similar properties to the Rayleigh-Taylor instability is viscous fingering, which occurs in a porous medium when a less viscous fluid is injected into a more viscous miscible fluid [15,16]. Pritchard [17] classified the stability of viscous fingering, including the equivalent form of a double-diffusive instability in which an instability occurs when a more viscous fluid is injected into a less viscous fluid. Nonlinear simulations by Mishra et al. [18] theoretically verified the existence of these instabilities. Both these instabilities can be induced by chemical reactions [19].

The stability of non-monotonic viscosity profiles was examined by [20,21], and nonlinear simulations by [22] verify the predictions. Previously Tan and Homsy [23] performed a linear stability analysis using the quasi-steady state approximation to derive an analytical dispersion equation for the case when the viscosity profile is given by a step function, which confirmed the result that an instability occurs whenever a less viscous fluid is injected into a more viscous fluid. Nonlinear simulations by [23] found that although using the quasi-steady state approximation within the linear stability analysis did not agree for small times, for intermediate times the linear stability analysis produced growth rates comparable with the nonlinear simulations. To overcome this small time failure, Ben et al. [24] used a spectral analysis method without using the quasi-steady state approximation within the linear stability analysis on viscous fingering. Using this spectral analysis method Kim [25] analysed viscous fingering of a miscible slice and compared the growth rates with those predicted using the quasi-steady approximation. At small times the two meth-

ods disagreed, but later in time they predicted similar growth rates. Hota et al. [26] employed the quasi-steady state approximation for the case of viscous fingering of a miscible slice in the presence of adsorption.

There are several studies which couple the bimolecular reaction $A+B \to C$ with Rayleigh-Taylor instabilities when the two reactants are initially partitioned. By analysing the large time asymptotic density profiles a total of 62 different types have been found [27], and clearly the same number of viscosity profiles are present in viscous fingering. Kim [28] performed the spectral analysis method and full numerical simulations to this problem in the case of equal diffusion coefficients, and later Kim [29] returned to this problem in the more general case of unequal diffusion coefficients. The corresponding viscous fingering instability was performed by Hejazi et al. [30] using the quasi-steady state approximation in the case of equal diffusion coefficients.

Studies on carbon dioxide sequestration typically introduce a species at the top of the domain and usually lead to a non-monotonic density profile. A linear stability analysis of the density-driven convection was performed by Riaz et al. [31] using the spectral analysis method and their predictions were confirmed by nonlinear simulations. The spectral analysis method along with full numerical simulations were recently applied by Kim et al. [32–34] to model carbon dioxide sequestration.

The study by Gandhi and Trevelyan [35] examined the initial onset conditions for a Rayleigh-Taylor instability for several different piecewise constant density profiles using the same approach as [23]. The study obtained implicit solutions for the dispersion equation and as all of the density profiles examined led to equivalent onset conditions involving the Rayleigh-Darcy number, a conjecture was made about the onset condition for more general density profiles. Kim [36] found that the growth rates obtained by the spectral analysis method did not agree with the results obtained by [35] for small times, but did agree with the quasi-steady state approximation at later times.

One notes that [14] performed a spectral analysis on the nonlinear simulations which involved taking the Fourier transform of the concentration in the vertical direction and then averaging them in the horizontal direction. This allowed the instantaneous growth rate to be obtained from the nonlinear simulations and compared with a linear stability analysis. They found, as expected, that the nonlinear simulations don't agree with the linear stability analysis for small times as the quasi steady state is not valid at small times since the base state solution initially changes very quickly in time. For moderate times the linear stability analysis was in reasonable agreement with the predictions from the nonlinear simulations. For large times the instability generated a fluid motion, thus the nonlinear simulations and linear stability analysis predictions for the growth rate diverged.

In this study we examine buoyancy instabilities in a two dimensional vertically oriented porous medium. The main focus is on using the quasi-steady state approximation to examine the onset condition for piecewise linear density profiles at times greater than zero, and full nonlinear simulations are performed to visualise the resulting instabilities. The presence of the species is assumed to

linearly affect the density of the fluid and various initial concentration profiles for a species dissolved in the fluid are considered.

In section 2 a mathematical model is non-dimensionalised, and using the stream function formulation, a linear stability analysis yields a system of two coupled differential equations. The problem is discretised and reduced to an eigenvalue problem. In section 3 we consider a step function concentration profile to validate the numerical approach. In section 4 we examine the stability of a species initially uniformly distributed in a finite layer. Finally, in section 5 we examine the stability of a species initially linearly distributed in a finite layer. We consider both a linear increasing density profile and a linear decreasing density profile. Within each section full numerical simulations are presented to demonstrate how the instability evolves. Finally, we draw our conclusions in section 6.

2 Model

Suppose that a species A is dissolved in a fluid contained inside a vertically orientated two dimensional homogeneous porous medium. We assume that the permeability K and porosity ϕ of the porous medium are constants. The fluid flow is assumed to satisfy Darcy's law and the concentration, a, of species A satisfies the mass transport equation, see Nield and Began [37]. For Darcy's law to be valid for flow in a porous medium it is required that the flow length scales are larger than the typical pore size, i.e. $\sqrt{K}$, so we require that the wave length of any instabilities are much larger than the pore size. We note that the validity of using Darcy's law in a Hele-Shaw cell was studied by Martin et al. [38]. The Darcy velocity $\underline{u}$ is the average fluid velocity per unit volume of the porous medium (including both solid and fluid material), which is different to the intrinsic velocity which is the average fluid velocity per unit volume occupied by the fluid. For simplicity we assume that the dispersion coefficient D of species A is a constant.

The density of the fluid ρ is taken to be a linear function of the concentration of species A, given by $\rho = \rho_0(1 + \alpha a)$ where ρ_0 is the density of the fluid in the absence of species A and α is the solutal expansion coefficient defined by $\alpha = (1/\rho_0)(d\rho/da)$. It is assumed that the concentration of the species is sufficiently small that the Boussinesq approximation is valid and so the flow can be considered incompressible, additionally variations in the viscosity of the fluid are assumed negligible, so μ, the dynamic viscosity, is a constant. The vertical coordinate x is chosen to increase in the downwards direction and $\underline{i}$ denotes the unit downwards pointing vector along the x axis.

This problem is modelled by the following two dimensional system of partial differential equations:

$$\underline{\nabla} \cdot \underline{u} = 0, \tag{1}$$

$$\underline{\nabla} p = -\frac{\mu}{K}\underline{u} + \rho_0 g(1+\alpha a)\underline{i}, \tag{2}$$

$$\phi\frac{\partial a}{\partial t} + \underline{u} \cdot \underline{\nabla} a = D\nabla^2 a \tag{3}$$

where p is the fluid's pressure, t is time and g is the magnitude of the acceleration due to gravity. We assume that initially the fluid is at rest and that the concentration of the species is given by

$$a(x, y, 0) = b_0 + a_0\overline{a}(x) \tag{4}$$

where y is the horizontal coordinate, b_0 is a reference concentration and a_0 is the difference between the initial maximum concentration and the reference concentration. We assume that vertically the physical domain is sufficiently large that it can be assumed infinite, so the far field conditions are

$$a_x \to 0 \quad \text{and} \quad \underline{u} \to \underline{0} \quad \text{as} \quad x \to \pm\infty. \tag{5}$$

2.1 Non-dimensionalisation

We non-dimensionalise the system by rescaling the variables as follows:

$$\underline{u} = \frac{D}{l_0}\underline{U}, \quad p = p_a + \rho_0 g l_0 X + \frac{\mu D}{K}P, \quad a = b_0 + a_0 A, \tag{6}$$

$$(x, y) = l_0(X, Y), \quad t = \frac{\phi l_0^2}{D}T \quad \text{where} \quad l_0 = \frac{\mu D}{\rho_0 g\alpha a_0 K} \tag{7}$$

and the atmospheric pressure is denoted by p_a. Here we are assuming that the presence of species A increases the density of the fluid, so $\alpha > 0$. Notice, increasing the reference concentration a_0 leads to a reduction in the length and time scales, and an increase in the velocity scale. Using these scalings we obtain the following dimensionless system of equations:

$$\underline{\nabla} \cdot \underline{U} = 0, \tag{8}$$

$$\underline{\nabla} P = -\underline{U} + A\underline{i}, \tag{9}$$

$$A_T + \underline{U} \cdot \underline{\nabla} A = \nabla^2 A. \tag{10}$$

The initial conditions are

$$\underline{U}(X, Y, 0) = \underline{0} \quad \text{and} \quad A(X, Y, 0) = \overline{A}(X) \tag{11}$$

where $\overline{A}(X) = \overline{a}(l_0 X)$. We note that if a profile has a dimensional thickness of h then the dimensionless thickness is

$$L = \frac{h}{l_0} = \frac{\rho_0 g\alpha a_0 h K}{\mu D} \tag{12}$$

which is the Rayleigh-Darcy number. The dimensionless far field conditions are now

$$A_X \to 0 \quad \text{and} \quad \underline{U} \to \underline{0} \quad \text{as} \quad X \to \pm\infty. \tag{13}$$

2.2 Stream Function Formulation

By introducing a stream function ψ, we can satisfy the conservation of mass equation (8), where the velocity is given by $\underline{U} = \underline{\nabla} \times \psi \underline{k}$, where $\underline{k}$ is the unit normal perpendicular to the vertical plane containing the porous medium. The velocity components are given by $U = \psi_Y$ and $V = -\psi_X$ where $\underline{U} = (U, V)$. By taking the curl of the dimensionless version of Darcy's law, equation (9), the pressure is eliminated and we obtain

$$\nabla^2 \psi = A_Y. \tag{14}$$

The mass transport equation (10) can now be expressed as

$$A_T + \psi_Y A_X - \psi_X A_Y = \nabla^2 A. \tag{15}$$

Notice that by moving to a stream function formulation the problem is reduced to two dependent variables ψ and A. The initial conditions are now

$$\psi_X(X, Y, 0) = \psi_Y(X, Y, 0) = 0, \quad \text{and} \quad A(X, Y, 0) = \overline{A}(X). \tag{16}$$

The far field conditions finally become

$$A_X \to 0 \quad \text{and} \quad \psi_X, \psi_Y \to 0 \quad \text{as} \quad X \to \pm\infty. \tag{17}$$

We will carry out a linear stability analysis on equations (14) and (15) along with the initial and far field conditions.

2.3 Full Numerical Simulation

Full numerical simulations were performed using the stream function formulation given by equations (14) and (15). Small scale random noise was added to the initial concentration, A. A multi-grid method [39] was used to solve equation (14) for the stream function ψ. The concentration A was obtained from the two-dimensional transport equation (15) by solving it in conservative form using the Lin-Rood method [40] with a third-order finite-difference operator [41].

2.4 Linear Stability Analysis

In the absence of an instability no fluid motion will take place and the species will diffuse. The base state solutions to this problem are denoted with tildes, i.e.

$$\tilde{\psi}(X,T) = 0 \quad \text{and} \quad \tilde{A}(X,T) \tag{18}$$

To perform a stability analysis we consider a small perturbation to the base states of the form

$$\psi = \epsilon\hat{\psi}(X,Y,T) \quad \text{and} \quad A = \tilde{A}(X,T) + \epsilon\hat{A}(X,Y,T) \tag{19}$$

where ϵ is a small constant. Substituting these expressions into equation (14) yields a perturbed version of Darcy's law:

$$\hat{\psi}_{XX} + \hat{\psi}_{YY} = \hat{A}_Y. \tag{20}$$

Similarly substituting the expressions into equation (15) yields, at leading order, an equation for the evolution of the base state concentration

$$\tilde{A}_T = \tilde{A}_{XX} \tag{21}$$

along with the far field boundary conditions

$$\tilde{A}_X \to 0 \quad \text{as} \quad X \to \pm\infty. \tag{22}$$

Next, at order $O(\epsilon)$ we have the perturbed mass transport equation, namely

$$\hat{A}_T + \hat{\psi}_Y\tilde{A}_X = \hat{A}_{XX} + \hat{A}_{YY}. \tag{23}$$

We now make the quasi steady state approximation that the base state solution is varying slower than the perturbations so that we can consider the base state solutions frozen in time. This means that the equations are now invariant under translation with regard to Y and T, so that the perturbations can be expressed in normal form as

$$[\hat{\psi}, \hat{A}] = \left[\frac{\mathrm{i}}{k}\mathcal{F}(X), \mathcal{A}(X)\right] \mathrm{e}^{\sigma T + \mathrm{i}kY} \tag{24}$$

where k is the wavenumber and σ is the instantaneous growth rate. Substituting these forms into equations (20) and (23) yields the following differential eigenvalue problem:

$$\mathcal{F}_{XX} = k^2(\mathcal{A} + \mathcal{F}), \tag{25}$$

$$\sigma\mathcal{A} = \mathcal{A}_{XX} - k^2\mathcal{A} + \mathcal{F}\tilde{A}_X \tag{26}$$

where σ is the eigenvalue and $\mathcal{A}$ and $\mathcal{F}$ are the eigenfunctions. The far field conditions for the eigenfunctions are

$$\mathcal{A}_X \to 0 \quad \text{and} \quad \mathcal{F}_X \to 0 \quad \text{as} \quad X \to \pm\infty. \tag{27}$$

Notice that equations (25), (26) and (27) are invariant under the transformation $X \to -X$, $\tilde{A} \to C - \tilde{A}$, $\mathcal{A} \to -\mathcal{A}$ and $\mathcal{F} \to -\mathcal{F}$, where C is an arbitrary constant. This means that the instantaneous growth rate σ for a concentration profile $\tilde{A} = G(X)$ is identical to that for the concentration profile $\tilde{A} = C - G(-X)$.

2.5 Numerical Linear Stability Analysis

In order to solve this differential eigenvalue problem we adapt the method introduced by Kalliadasis *et al.* [42] to this problem. We truncate the problem to a finite domain and discretise X to a set of n non-uniformly distributed spatial points, X_1, X_2, ..., X_n. The distribution of the X_i's are given in appendix A. The eigenfunctions $\mathcal{A}$ and $\mathcal{F}$ are then expressed using eigenvectors $\underline{v_A}$ and $\underline{v_F}$, written as

$$\underline{v_A} = \begin{pmatrix} A_1 \\ A_2 \\ \vdots \\ A_n \end{pmatrix} \quad \text{and} \quad \underline{v_F} = \begin{pmatrix} F_1 \\ F_2 \\ \vdots \\ F_n \end{pmatrix}. \tag{28}$$

We also introduce the diagonal matrix

$$\underline{\underline{J}} = \begin{pmatrix} \tilde{A}_X|_{X_1} & 0 & \cdots & 0 \\ 0 & \tilde{A}_X|_{X_2} & \cdots & 0 \\ \vdots & \vdots & \ddots & \vdots \\ 0 & 0 & \cdots & \tilde{A}_X|_{X_n} \end{pmatrix}. \tag{29}$$

In appendix B we present a matrix $\underline{\underline{S}}$, which was obtained using finite difference approximations to be a third order accurate approximation of the second derivative, such that

$$\frac{d^2\underline{\Phi}}{dX^2} \approx \underline{\underline{S}}\ \underline{\Phi}\ . \tag{30}$$

Hence, we were able to approximate equations (25) and (26) by

$$\underline{\underline{S}}\ \underline{v_F} = k^2(\underline{v_A} + \underline{v_F}), \tag{31}$$

$$\sigma\underline{v_A} = \underline{\underline{S}}\ \underline{v_A} - k^2\underline{v_A} + \underline{\underline{J}}\ \underline{v_F}. \tag{32}$$

Then equation (31) can then be written as

$$\underline{\underline{Q}}\ \underline{v_F} = k^2\underline{v_A} \quad \text{where} \quad \underline{\underline{Q}} = \underline{\underline{S}} - k^2\underline{\underline{I}} \tag{33}$$

where $\underline{\underline{I}}$ is the $n \times n$ identity matrix. Multiplying this equation by $\underline{\underline{Q}}^{-1}$ yields

$$\underline{v_F} = k^2\underline{\underline{Q}}^{-1}\underline{v_A}. \tag{34}$$

Substituting this expression for $\underline{v_F}$ into equation (32) yields

$$\sigma\underline{v_A} = \underline{\underline{Q}}\ \underline{v_A} + k^2\underline{\underline{J}}\ \underline{\underline{Q}}^{-1}\underline{v_A}. \tag{35}$$

Then we can write the system as

$$\sigma\underline{v_A} = \underline{\underline{M}}\ \underline{v_A} \quad \text{where} \quad \underline{\underline{M}} = \underline{\underline{Q}} + k^2\underline{\underline{J}}\ \underline{\underline{Q}}^{-1}. \tag{36}$$

By solving this eigenvalue problem for σ and $\underline{v_A}$ over a range of wavenumbers k we can obtain dispersion curves. When using n spatial points, the cpu time

of the code approximately scaled with $n^{2.5}$. Typically 401 spatial points were used over domains of various sizes to ensure that grid independent results were obtained, however, more grid points were required when a very large domain was required in the presence of sharp profiles, for example at small times when large gradients are present, or when obtaining neutral stability curves. Additionally, the domain size was chosen to be greater than $8\pi/k$ to avoid the boundary conditions dampening any instabilities.

In the following sections we will use this numerical linear stability analysis approach to obtain the instantaneous growth rates for a range of different base state concentration profiles.

3 A step function

First we consider the case when the initial distribution of species A is a step function profile with a maximum concentration of 1, centred at $X = 0$, i.e.

$$\tilde{A}(X,0) = \begin{cases} 1, & \text{for } X < 0 \\ 0, & \text{for } X > 0 \end{cases}. \tag{37}$$

Physically this corresponds to species A being uniformly dissolved in the upper half of the domain, with species A being absent from bottom half of the domain. At time $T = 0$ the instantaneous growth rate is given by

$$\sigma = \frac{k}{2}\left(1 - k - \sqrt{k(k+2)}\right) \tag{38}$$

which was obtained by Tan and Homsy [23] for a miscible viscous displacement. The largest positive value of k that satisfies $\sigma = 0$ defines the cut off wavenumber, so that all wavenumbers greater than this value result in $\sigma < 0$ and the system being stable. The fastest growing wavenumber is the value of k when σ reaches its maximum value. [23] found that the cut off wavenumber is given by $k_{\text{cut}} = 1/4$ and the fastest growing wavenumber is $k_{\max} = (\sqrt{5}-2)/2$ with the maximum instantaneous growth rate given by $\sigma_{\max} = (5\sqrt{5}-11)/8$. This unstable system corresponds to a more dense fluid overlying a less dense fluid.

In order to obtain the instantaneous growth rate at later times we perform a numerical linear stability analysis. Now the base state concentration needs to satisfy equations (21) and (22) along with the initial condition

$$\tilde{A}(X,0) = H(-X) \tag{39}$$

where H is the Heaviside step function. This system can be solved to yield

$$\tilde{A}(X,T) = \frac{1}{2} - \frac{1}{2}\text{erf}\left(\frac{X}{2\sqrt{T}}\right) \tag{40}$$

which is a self-similar solution in which the profile for $\tilde{A}$ spreads out in the X direction with the square root of time. We notice that the most negative gradient is $-(4\pi T)^{-1/2}$ which occurs at $X = 0$.

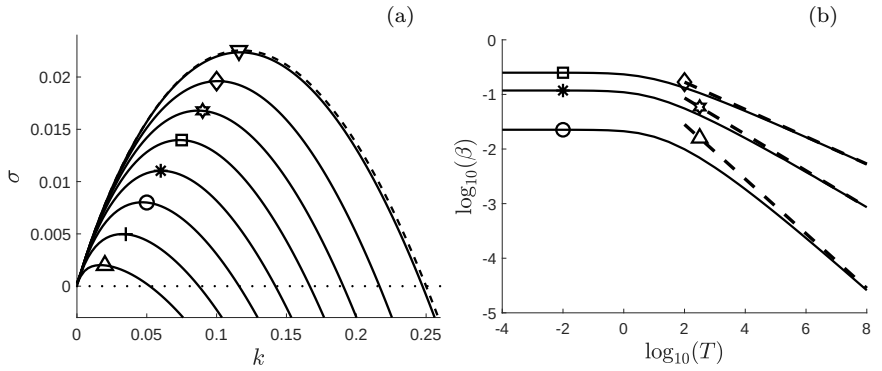

Fig. 1 In (a) dispersion curves of the instantaneous growth rate σ are plotted against the wavenumber k for an initial step function profile, obtained using equations (36) and (40). Curves are illustrated at times $T = 0.01$ ($\triangledown$), 3 ($\diamond$), 10 ($\star$), 26 ($\square$), 68 ($*$), 200 ($\bigcirc$), 800 ($+$) and 8000 ($\triangle$). The dashed line is at time $T = 0$ given by the analytical solution in equation (38). In (b) log-log plots in time are illustrated where $\beta = \sigma_{\max}$ ($\bigcirc$), $\beta = k_{\max}$ ($*$), $\beta = k_{\text{cut}}$ ($\square$), $\beta = (4\pi T)^{-1/2}$ ($\triangle$), $\beta = 0.4T^{-1/3}$ ($\star$), and $\beta = (4\pi T)^{-1/4}$ ($\diamond$).

A numerical linear stability analysis was carried out by obtaining the maximum eigenvalue σ of the matrix $\underline{\underline{M}}$ given by equation (36) over a range of wavenumbers k, where the matrix $\underline{\underline{J}}$ uses the spatial derivative of the base state concentration which can be analytically obtained from equation (40).

At time $T = 0$ the dispersion curve, corresponding to an initial step function profile, given by equation (38) is illustrated in figure 1(a). Typical dispersion curves obtained from the numerical linear stability analysis are present at later times in figure 1(a). We notice that the dispersion curve at time $T = 0.01$ is close to the analytical solution (38) at time $T = 0$, which suggests that the numerical approach employed is sufficiently accurate. Figure 1(a) shows that as T increases, the maximum instantaneous growth rate $\sigma_{\max}$, the fastest growing wavenumber $k_{\max}$, and the cut off wavenumber k_{cut}, all decay, which means that although the system remains unstable in time, the range of unstable wavenumbers is decreasing and the wavelength will increase in time.

In appendix C we use equations (25) and (26) to show that for large times T the maximum instantaneous growth rate and cut off wavenumber approach

$$\sigma_{\max} \approx (4\pi T)^{-1/2} \quad \text{and} \quad k_{\text{cut}} \approx (4\pi T)^{-1/4}. \tag{41}$$

These large time asymptotic predictions are illustrated in figure 1(b). Using a log-log plot we illustrate the time evolution of the maximum growth rate $\sigma_{\max}$, the fastest growing wavenumber $k_{\max}$ and the cut off wavenumber k_{cut} obtained from the numerical linear stability analysis, in figure 1(b). We observe that for small T, typically less than 1, the maximum instantaneous growth rate $\sigma_{\max}$, the fastest growing wavenumber $k_{\max}$, and the cut off wavenumber k_{cut} are approximately constant. All of these quantities decay in time T.

In figure 1(b) we see that the numerical solution for $\sigma_{\max}$ and k_{cut} denoted using the $\bigcirc$ and $\square$ symbols, respectively, each approach their respective large

i	T_i	$k_{\max}$	$2\pi/k_{\max}$
1	101.35	0.0551	114.0
2	277.18	0.0431	145.8
3	513.28	0.0367	171.2

Table 1 Numerically obtained values of T_i defined by equation (42) for an initial step function profile.

time asymptotic solutions (41) denoted using the $\triangle$ and $\diamond$ symbols. Additionally, we see that $k_{\max}$ denoted by the $*$ symbol approximately tends to $0.4T^{-1/3}$ denoted by the $\star$ symbol.

We numerically find that product $\sigma_{\max}T$ is a monotonic increasing function of T which scales with $\sqrt{T}$ for large time. Thus, for large times $\sigma T \to \omega\sqrt{T}$ where ω is a constant. Hence, for an initial step function concentration profile, the eigenfunctions and length of the fingers scale with $e^{\omega\sqrt{T}}$ for large times.

It is important to note that as we are using the quasi-steady state approximation, the instantaneous growth rates obtained at small times are not valid, however, for times of $O(1)$ and later the instantaneous growth rates are more relevant. However, once an instability occurs, fluid motion will set in and dramatically change the base state concentration profile meaning that the results later in time will no longer be valid. Hence, the linear stability analysis is typically most useful around the time when the product of the maximum instantaneous growth rate with time is around $O(1)$. Hence, we introduce the time T_i, defined as the time T that satisfies

$$T\sigma_{\max} = i \tag{42}$$

which is a generalised version of the notation introduced by [14] who used $i = 1$. In table 1 we present numerically obtained values for T_i for $i = 1$, 2 and 3. Using the value for T_1 in table 1, we see that the the linear stability is predicting that an instability will emerge around $T \approx 100$ with a wavelength around 114. To verify this prediction we carried out full numerical simulations by solving equations (14) and (15) with an initial step function concentration profile. The instability was still very weak at time T_1 and so we present the solution later in time in order to be able to visualise the instability. In figure 2 we illustrate contours of the concentration A at times $T = 400$ and $T = 1200$. In figure 2 the darker shaded regions have higher concentrations of species A and the lighter shaded regions have lower concentrations of species A, and we recall that the X axis increases in the downwards direction. As expected, long narrow fingers are seen to develop in time and sink downwards. We notice at time $T = 1200$ we see 12 fingers falling downwards in a domain of thickness 1500, so the thickness of each finger is around 125. Hence, the observed wavelengths are consistent with those predicted in table 1.

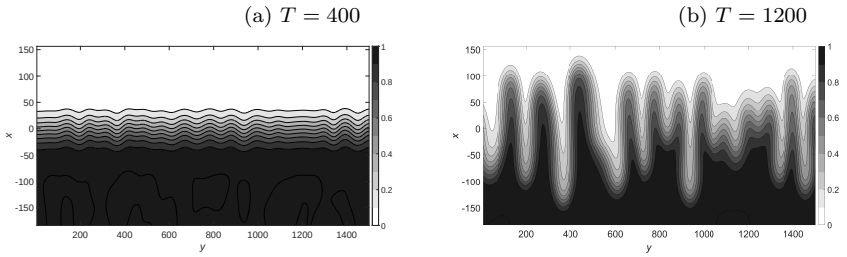

Fig. 2 Contours of A obtained from equations (14) and (15) with an initial condition corresponding to a step function profile at times (a) $T = 400$ and (b) $T = 1200$.

4 A finite layer

Next we consider the case when the initial distribution of species A is a layer of thickness L with a maximum concentration of 1, centred at $X = 0$, i.e.

$$\tilde{A}(X,0) = \begin{cases} 0, & \text{for } 2X < -L \\ 1, & \text{for } -L < 2X < L \\ 0, & \text{for } L < 2X \end{cases} . \tag{43}$$

Physically this corresponds to species A being uniformly dissolved in a layer of thickness L, with species A being absent from both the regions above and below this layer. At time $T = 0$ the instantaneous growth rate satisfies

$$\frac{4\sigma^2}{k^2} = 1 - e^{-2kL} - \frac{2k}{s}\left(1 - e^{-(k+s)L}\right) + \frac{k^2}{s^2}\left(1 - e^{-2sL}\right) \tag{44}$$

where $s^2 = \sigma + k^2$ which was obtained by [35]. Typical dispersion curves at time $T = 0$ are illustrated in figure 3(a) for various values of L using equation (44). We notice that increasing L leads to an increase in the growth rate σ, but the step function profile given by equation (38) is an upper bound to the growth rate. We note that the cut off wavenumber satisfies

$$(1 + kL)e^{-kL} = \sqrt{1 - 16k^2}. \tag{45}$$

It was shown in [35] that this system is unstable when

$$L > 4 \tag{46}$$

at time $T = 0$.

In order to obtain the instantaneous growth rate at later times we perform a numerical linear stability analysis. Now the base state concentration needs to satisfy equations (21) and (22) along with the initial condition

$$\tilde{A}(X,0) = H(L^2 - 4X^2). \tag{47}$$

Solving this system yields the base state concentration

$$\tilde{A}(X,T) = \frac{1}{2}\left[\operatorname{erf}\left(\frac{2X + L}{4\sqrt{T}}\right) - \operatorname{erf}\left(\frac{2X - L}{4\sqrt{T}}\right)\right]. \tag{48}$$

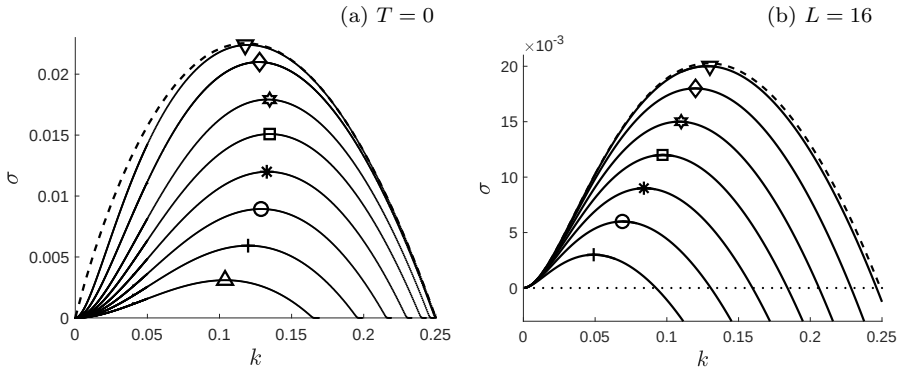

Fig. 3 Dispersion curves of the instantaneous growth rate σ against the wavenumber k for an initial profile of a layer of thickness L. In (a) curves are illustrated at $T = 0$, obtained from the analytical solution to equation (44), for layers of thicknesses $L = 5.8$ ($\triangle$), 6.7 ($+$), 7.7 ($\bigcirc$), 8.9 ($*$), 10.5 ($\square$), 12.7 ($\star$), 17.8 ($\diamond$) and 28.8 ($\triangledown$). The dashed line is for an initial step function profile at $T = 0$ given by equation (38). In (b) curves are illustrated for a finite layer of thickness $L = 16$, obtained using equations (36) and (48), at times $T = 68.18$ ($+$), 28.39 ($\bigcirc$), 14.93 ($*$), 8.06 ($\square$), 3.88 ($\star$), 1.22 ($\diamond$), and 0.1 ($\triangledown$). The dashed line corresponds to the analytical solution (44) at $T = 0$.

Initially $\tilde{A}$ remains fairly flat and close to 1 around $X = 0$, however, eventually the profile spreads out and the maximum value decays to zero. The maximum concentration of $\tilde{A}$ is $\text{erf}\left(\frac{L}{4\sqrt{T}}\right)$ which occurs at $X = 0$. The maximum concentration falls by less than 1% as long as $L \geq 4\sqrt{T}\text{erf}^{-1}(0.99) \approx 7.286\sqrt{T}$. The total amount of $\tilde{A}$ present is $\int_{-\infty}^{\infty} \tilde{A} dX = L$. A useful measure of how the profile changes in time is to consider $\int_{-L/2}^{L/2} \tilde{A}\ dX$ which remains above 85% of the initial value of L when $L \geq 7.523\sqrt{T}$.

The numerical linear stability analysis was carried out by obtaining the maximum eigenvalue σ of the matrix $\underline{\underline{M}}$ given by equation (36) over a range of wavenumbers k, where the matrix $\underline{\underline{J}}$ uses the spatial derivative of the base state concentration which can be analytically obtained from equation (48). Typical dispersion curves for a layer of thickness $L = 16$ are illustrated in figure 3(b) at various times. We notice that at time $T = 0.1$ the dispersion curve is close to the analytical dispersion curve (44) at $T = 0$. As time increases the growth rates monotonically decrease.

Numerically we find that close to criticality the growth rate appears to approximately scale with $(L - 4)^3/T$, so in figure 4(a) we plot the one third power of the product of the maximum instantaneous growth rate with time against L at various times. We notice that as L tends to 4 the maximum instantaneous growth rate tends to zero, indicating that the system is stable for $L \leq 4$. Hence, numerically we have found that the condition for an instability

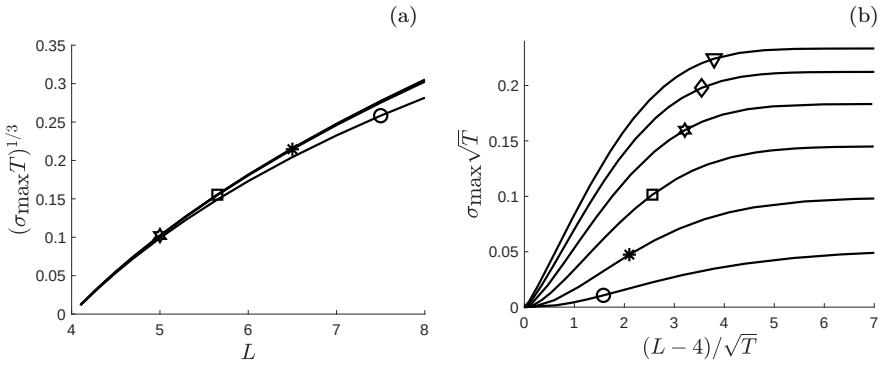

Fig. 4 Properties of the maximum instantaneous growth rate for an initial profile of a layer of thickness L obtained by numerically solving equations (36) and (48). In (a) curves of one third power of the product of the maximum instantaneous growth rate $\sigma_{\max}$ with time T are plotted against L, at times $T = 10$ ($\bigcirc$), 10^2 ($*$), 10^3 ($\square$) and 10^4 ($\star$). In (b) curves of the maximum instantaneous growth rate multiplied by the square root of time are plotted against $(L-4)$ divided by the square root of time, at times $T = 10$ ($\bigcirc$), 10^2 ($*$), 10^3 ($\square$), 10^4 ($\star$), 10^5 ($\diamond$) and 10^6 ($\triangledown$).

of a finite layer of thickness L and maximum concentration 1 evolving in time is the same as condition (46) found by [35] at $T = 0$.

In figure 4(b) the product of the maximum instantaneous growth rate with the square root of time is plotted against $(L-4)/\sqrt{T}$ at various times. We notice that for a fixed value of T, as L increases the maximum instantaneous growth rates increases but approaches a constant for $(L-4)$ sufficiently greater than $\sqrt{T}$. As we increase L, the finite layer is getting thicker and so we should expect the growth rates to tend to those obtained for a step function profile, and so they should tend to a constant.

In figure 5(a) we plot $\log_{10}(L)$ against $\log_{10}(T_i)$ for $i = 1$, 2 and 3. We observe that the value of each T_i tends to a constant as L tends to infinity, however, as L decreases towards a critical value, each T_i tends to infinity. For a given value of L we see that $T_1 < T_2 < T_3$.

Figure 5(b) shows $\log_{10}(\sigma_{\max})$ plotted against $\log_{10}(T)$ for various L. We see that for very small times the growth rates are constant, but as time increases the growth rates decrease. For moderate times, when $L = 10^2$, 10^3, 10^4 and 10^5, we see that the maximum instantaneous growth rates are the same as for a single step, however, for large times, the growth rates eventually decay away from the maximum instantaneous growth rates of a single step. We see that the larger the value of L the longer the growth rates for a finite layer resemble the growth rates for a finite step. Figure 5(b) shows that the gradients of the logarithms of the growth rates against the logarithm of time are -1 for the finite layer and $-1/2$ for a single step. Hence, we have numerically found that, for thick layers, the growth rates for a finite layer are initially constant, then decay with $T^{-1/2}$ (like a single step), and then even later in time decay like T^{-1}. When the growth rate decays like T^{-1}, this means that

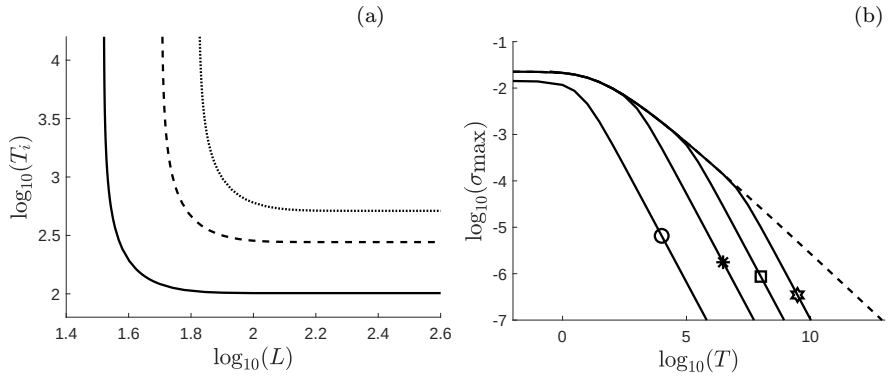

Fig. 5 Log-log plots for an initial profile of a layer of thickness L obtained by numerically solving equations (36) and (48). In (a) $\log_{10}(L)$ is plotted against $\log_{10}(T_i)$ for $i = 1$, 2 and 3. The solid line corresponds to T_1, the dashed line to T_2 and the dotted line to T_3. In (b) $\log_{10}(\sigma\max)$ is plotted against $\log_{10}(T)$ for $L = 10$ ($\bigcirc$), 10^2 ($*$), 10^3 ($\square$) and 10^4 ($\star$). The dashed curve corresponds to an initial profile of a step function.

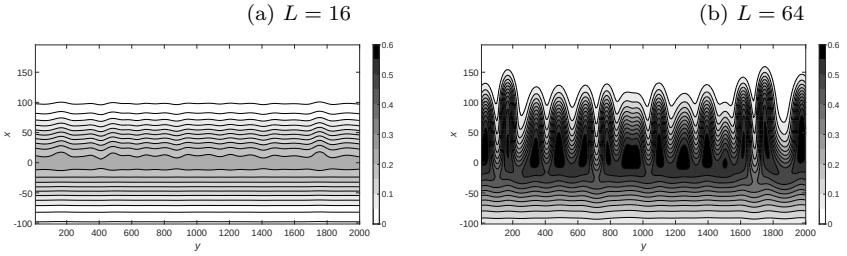

Fig. 6 Contours of A obtained from equations (14) and (15) with an initial condition corresponding to a finite layer of thickness (a) $L = 16$ and (b) $L = 64$ at time $T = 10^3$.

the term σT is now constant in time, which corresponds to an instability with algebraic growth instead of exponential growth, as the problem is now in a much weaker regime. Hence, when a species is initially uniformly dissolved in a finite layer, the eigenfunctions and length of the fingers scale with T^p for large times, where p is a constant. This result should actually be expected for a finite layer as once the profile has diffused enough, the profile is almost flat and so there are no significant regions where we have a heavy region over a light region.

By performing numerical simulations the full solutions to equations (14) and (15) for an initial concentration profile corresponding to a finite layer of thickness L were obtained. Figure 6 shows contours of the concentration at time $T = 10^3$ for (a) $L = 16$ and (b) $L = 64$. Figure 6(b) for a thickness of $L = 64$ shows an instability which is significantly more pronounced than in figure 6(a) for a thickness of $L = 16$, as expected from the numerical linear stability analysis. These nonlinear simulations show that the thickness of a finite layer needs to be much larger than the critical thickness of $L = 4$ in

order to be able to visualise these instabilities. Additionally, as expected, the development of the instability for a finite layer shown in figure 6 is weaker than found for a single step shown in figure 2.

For $L = 64$, numerically we find that the linear stability predicts that $T_1 = 105.59$ and $T_2 = 442.88$. At these times the fastest growing wavenumbers are $k_{\max} = 0.0565$ and 0.0388 which give wavelengths of 111.2 and 161.9, respectively. In figure 6(b) at time $T = 10^3$ we see 14 fingers falling downwards in a domain of thickness 2000, so the thickness of each finger is around 143, so the numerically observed wavelengths are consistent with those predicted by the linear stability analysis.

5 A piecewise linear profile

Finally, we consider the case when the initial distribution of species A is a piecewise linear profile with concentrations of R_1 at $X = -L/2$ and R_2 at $X = L/2$, i.e.

$$\tilde{A}(X,0) = \begin{cases} 0, & \text{for } 2X < -L \\ \dfrac{1}{2}(R_1 + R_2) + \dfrac{X}{L}(R_2 - R_1), & \text{for } -L < 2X < L \\ 0, & \text{for } L < 2X \end{cases} \tag{49}$$

which physically corresponds to species A being dissolved in a layer of thickness L, such that the concentration is spatially linear, i.e. has a constant concentration gradient, with species A being absent from both the regions above and below this layer. At time $T = 0$ the analytical dispersion equation is given in appendix D, but the implicit solution is quite complicated and so only a single dispersion curve has been included in this study. The evolution of the base state satisfies equations (21) and (22) along with the initial condition

$$\tilde{A}(X,0) = \frac{1}{2L}\left[R_1\left(L - 2X\right) + R_2\left(L + 2X\right)\right] H(L^2 - 4X^2). \tag{50}$$

Solving this system yields the base state concentration

$$\begin{aligned} \tilde{A}(X,T) = {} & \frac{1}{4L}\left[R_1\left(L - 2X\right) + R_2\left(L + 2X\right)\right]\left[\operatorname{erf}\left(\frac{2X + L}{4\sqrt{T}}\right) - \operatorname{erf}\left(\frac{2X - L}{4\sqrt{T}}\right)\right] \\ & + (R_2 - R_1)\frac{\sqrt{T}}{L\sqrt{\pi}}\left[\exp\left(-\frac{(2X + L)^2}{16T}\right) - \exp\left(-\frac{(2X - L)^2}{16T}\right)\right]. \end{aligned} \tag{51}$$

The total amount of $\tilde{A}$ present is $\displaystyle\int_{-\infty}^{\infty} \tilde{A} dX = (R_1 + R_2)L/2$. After numerically exploring the parameter space we find that for large times the condition for an instability for the evolution of the piecewise linear profile (50) is

$$|R_1 + R_2|L > 8 \tag{52}$$

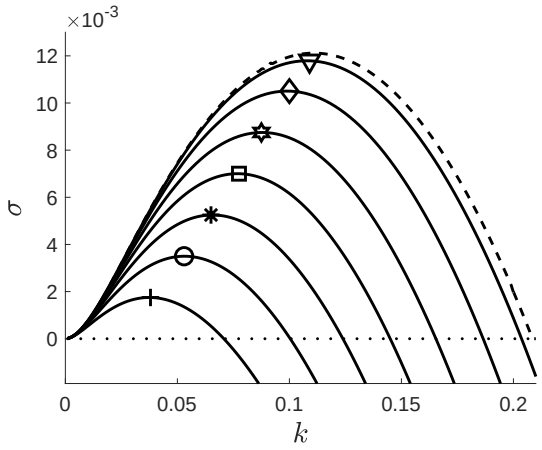

Fig. 7 Dispersion curves of the instantaneous growth rate σ against the wavenumber k for the initial piecewise linear profile (50) with a thickness of $L = 32$, obtained using equations (36) and (51). Here $R_1 = 0$ and $R_2 = 1$, corresponding to a bottom heavy triangular profile. Curves are illustrated at times $T = 108.37$ (+), 41.36 (◯), 19.74 (∗), 9.68 (□), 4.37 (⋆), 1.44 (◇) and 0.21 (▽). The dashed curve is at time $T = 0$ given by the analytical solution in appendix D.

which agrees with the conjecture made by [35] that the system is stable to long wave instabilities when

$$\left| \int_{-\infty}^{\infty} \tilde{A} dX \right| \leq 4 \quad \text{when} \quad \tilde{A} \to 0 \quad \text{as} \quad X \to \pm\infty. \tag{53}$$

The numerical linear stability analysis was carried out by obtaining the maximum eigenvalue σ of the matrix $\underline{\underline{M}}$ given by equation (36) over a range of wavenumbers k, where the matrix $\underline{\underline{J}}$ uses the spatial derivative of the base state concentration which can be analytically obtained from equation (51).

5.1 Increasing gradients − Bottom heavy triangular profiles

In this subsection, we consider $R_1 = 0$ and $R_2 = 1$ so that we initially have a bottom heavy triangular profile. The profile for $\tilde{A}$ changes rapidly near $X = L/2$ where the gradient is initially most negative. A useful measure is to consider $\displaystyle\int_0^{L/2} \tilde{A}\, dX$ which remains above 90% of the initial value of $3L/8$ when $L \geq 15.884\sqrt{T}$.

Typical dispersion curves for the evolution of the piecewise linear profile (50) with $R_1 = 0$, $R_2 = 1$, and $L = 32$, corresponding to a bottom heavy triangular profile, are illustrated in figure 7 at various times. We observe that the analytical dispersion curve at $T = 0$, given in appendix D, is close to

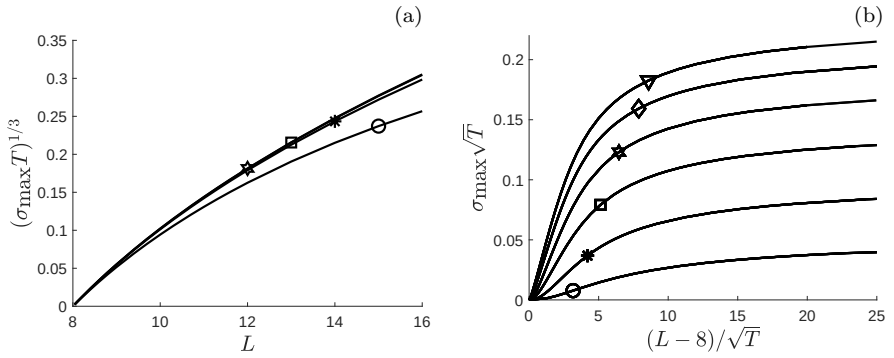

Fig. 8 Properties of the maximum instantaneous growth rate for the initial piecewise linear profile (50) with thickness L for $R_1 = 0$ and $R_2 = 1$, corresponding to a bottom heavy triangular profile, obtained by numerically solving equations (36) and (51). In (a) curves of one third power of the product of the maximum instantaneous growth rate $\sigma_{\max}$ with time T are plotted against L, at times $T = 10$ ($\bigcirc$), 10^2 ($*$), 10^3 ($\square$) and 10^4 ($\star$). In (b) curves of the maximum instantaneous growth rate multiplied by the square root of time are plotted against $(L-8)$ divided by the square root of time, at times $T = 10$ ($\bigcirc$), 10^2 ($*$), 10^3 ($\square$), 10^4 ($\star$), 10^5 ($\diamond$) and 10^6 ($\triangledown$).

the numerically obtained dispersion curve at $T = 0.21$. As time increases the growth rates decay.

Numerically we find that close to criticality the growth rate appears to approximately scale with $(L-8)^3/T$. In figure 8(a) the one third power of the product of the maximum instantaneous growth rate with time for the evolution of the piecewise linear profile (50) for $R_1 = 0$ and $R_2 = 1$, corresponding to a bottom heavy profile, is plotted against L at various times T. We notice that as L tends to 8 the maximum instantaneous growth rate tends to zero, indicating that the system is stable for $L \leq 8$, which agrees with the prediction in equation (52) for large times.

In figure 8(b) the product of the maximum instantaneous growth rate with the square root of time is plotted against $(L-8)/\sqrt{T}$ at various times for $R_1 = 0$ and $R_2 = 1$. We notice that for a fixed value of T, as L increases the maximum instantaneous growth rates increases.

When $R_1 = 0$ and $R_2 = 1$, in figure 9 we plot $\log_{10}(L)$ against $\log_{10}(T_i)$ for $i = 1$, 2 and 3. We see in figure 9 that the value of each T_i tends to a constant as L tends to infinity, however, as L decreases towards a critical value, each T_i tends to infinity. For a given value of L we see that $T_1 < T_2 < T_3$.

By performing numerical simulations we obtained the full solutions to equations (14) and (15) for an initial concentration corresponding to the piecewise linear profile (50) with thickness L for $R_1 = 0$ and $R_2 = 1$, corresponding to a bottom heavy triangular profile, see figure 10. Figure 10 shows contours of the concentration at time $T = 10^3$ for (a) $L = 32$ and (b) $L = 128$. Figure 10(b), for a thickness of $L = 128$, shows an instability which is significantly more pronounced than in figure 10(a) for a thickness of $L = 32$, as expected from the numerical linear stability analysis.

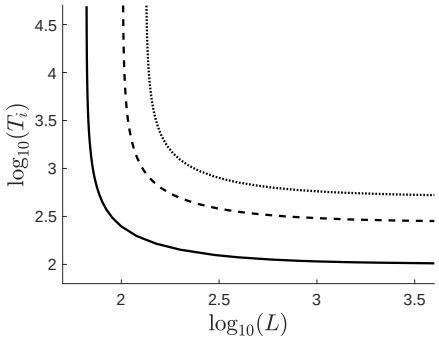

Fig. 9 Log-log plots relating T_i with L are presented for the initial piecewise linear profile (50) with thickness L with $R_1 = 0$ and $R_2 = 1$, corresponding to a bottom heavy triangular profile, obtained by numerically solving equations (36) and (51). The solid line corresponds to T_1, the dashed line to T_2 and the dotted line to T_3.

(a) $L = 32$ (b) $L = 128$

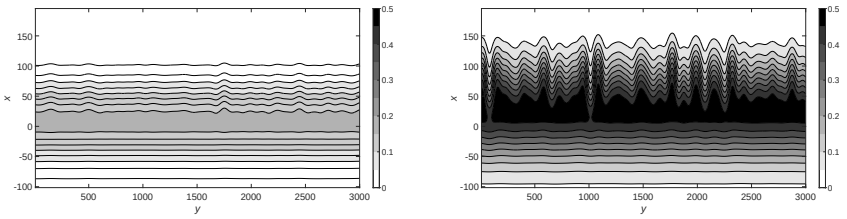

Fig. 10 Contours of A obtained from equations (14) and (15) with an initial condition corresponding to the piecewise linear profile (50) with $R_1 = 0$ and $R_2 = 1$, corresponding to a bottom heavy triangular profile, of thickness (a) $L = 32$ and (b) $L = 128$ at time $T = 10^3$.

For $L = 128$, $R_1 = 0$ and $R_2 = 1$ numerically we find that the linear stability predicts that $T_1 = 185.73$ and $T_2 = 1007.6$. At these times the fastest growing wavenumbers are $k_{\max} = 0.0446$ and 0.0259 which give wavelengths of 140.9 and 242.6, respectively. We note that in this case the wavelengths have a large range due to the large difference between T_1 and T_2. In figure 10(b) at time $T = 10^3$ we see 19 fingers falling downwards in a domain of thickness 3000, so the thickness of each finger is around 158, so the numerically observed wavelengths are consistent with those predicted by the linear stability analysis at time T_1.

5.2 Increasing gradients − Bottom heavy profiles

In this subsection, we consider $R_2 = 1$ with $|R_1| \leq 1$, so that the density is greatest at $X = L/2$, i.e. at the bottom of the layer. In figure 11 we present the neutral stability curves at various times when $R_2 = 1$, corresponding to a bottom heavy profile. For $R_1 \geq 0$ the marginal stability curve was not observed to

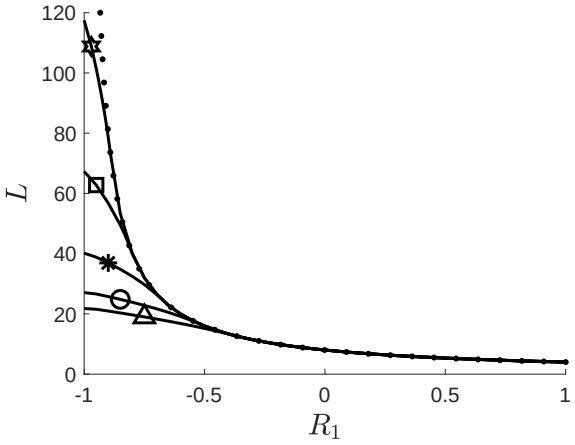

Fig. 11 Neutral stability curves for the initial piecewise linear profile (50) with thickness L and $R_2 = 1$, corresponding to a bottom heavy profile, obtained by numerically solving equations (36) and (51). Curves are illustrated at times $T = 0.001$ ($\triangle$), 10 ($\bigcirc$), 10^2 ($*$), 10^3 ($\square$) and 10^4 ($\star$). The dotted curve is the large time theoretical onset condition (52) with $R_2 = 1$.

change in time, however, for $R_1 < 0$, the marginal stability curve does change in time. Numerically we found that the system was stable to long wave instabilities when $|R_1 + R_2|L < 8$, however, short wave instabilities are found to be present when $|R_1+R_2|L < 8$, however, the region where these short wave instabilities occurs, shrinks in time. Hence, the neutral stability curve approaches the theoretically predicted condition (52) for large times. For small and moderate times when $R_1 < 0$ we numerically find that the threshold thickness can be significantly smaller than than thickness L predicted by equation (52) due to the presence of short wave instabilities.

When $R_1 = -1$ and $R_2 = 1$, in figure 12 we plot $\log_{10}(L)$ against $\log_{10}(T_i)$ for $i = 1$, 2 and 3. We observe that the value of each T_i tends to a constant as L tends to infinity. However, for moderate values of L, the T_i curves turn back of themselves, i.e. there exist values of L in which there are two values of T_i for $i = 1$, 2 and 3. As T_i satisfies $\sigma_{\max} T_i = i$, this means that the value of $\sigma_{\max} T$ is no longer monotonic increasing, but instead changes from initially being increasing in time to decreasing in time, so the system becomes less unstable in time. This result is expected, as the onset condition for an instability, equation (52), predicts that for large times the system will eventually be stable as $R_1 + R_2 = 0$.

In figure 13 we present contours of the maximum instantaneous growth rate for the evolution of the piecewise linear profile (50) when $R_2 = 1$, corresponding to a bottom heavy profile, at $T = 10$ and $T = 10^3$. Similar contours plots were found at other times but are not presented to avoid repetition. Although figure 13(a) at $T = 10$ resembles figure 13(b) at $T = 10^3$, we notice that the values of L are around 4 times larger. The contours show that increasing L

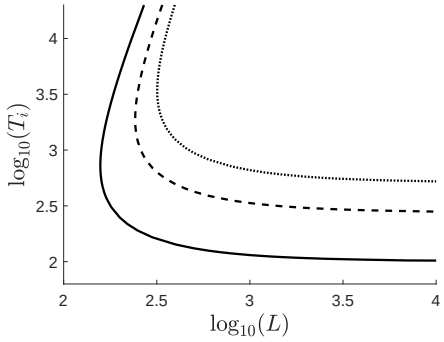

Fig. 12 Log-log plots relating T_i with L are presented for the initial piecewise linear profile (50) with thickness L with $R_1 = -1$ and $R_2 = 1$,corresponding to a bottom heavy profile, obtained by numerically solving equations (36) and (51). The solid line corresponds to T_1, the dashed line to T_2 and the dotted line to T_3.

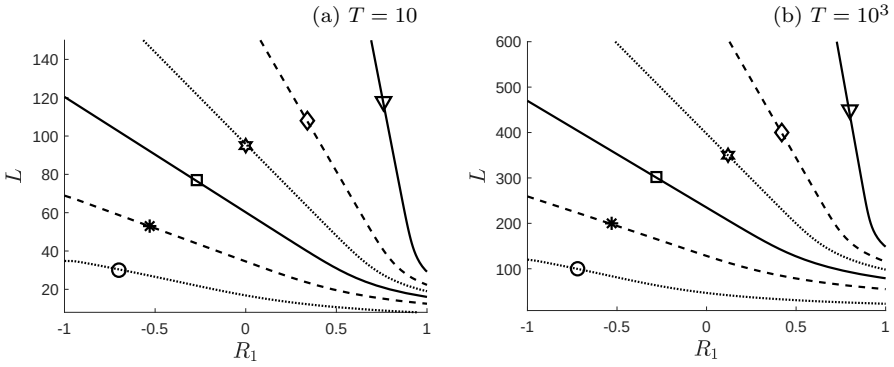

Fig. 13 Contours of the maximum instantaneous growth rate for the initial piecewise linear profile (50) for $R_2 = 1$, corresponding to a bottom heavy profile, obtained by numerically solving equations (36) and (51). In (a) $T = 10$ and contours are illustrated for $\sigma_{\max} = 0.002$ ($\bigcirc$), 0.0075 ($*$), 0.011 ($\square$), 0.013 ($\star$), 0.0145 ($\diamond$), 0.016 ($\triangledown$). In (b) $T = 10^3$ and contours are illustrated for $\sigma_{\max} = 0.0005$ ($\bigcirc$), 0.002 ($*$), 0.003 ($\square$), 0.0036 ($\star$), 0.004 ($\diamond$), 0.0044 ($\triangledown$).

and increasing R_1 both monotonically increase the maximum instantaneous growth rate at each of the times investigated. However, increasing T decreases the maximum instantaneous growth rate.

To summarise, numerically we have found that, for thick layers, the growth rates for the initial piecewise linear profile (50), when we have a bottom heavy profile, decay with $T^{-1/2}$ (like a single step) for a long time, however, later they decay like T^{-1}.

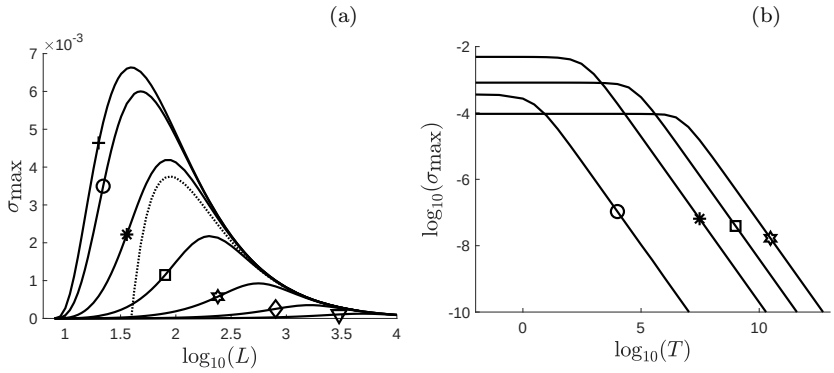

Fig. 14 Maximum instantaneous growth rates for the initial piecewise linear profile (50) obtained using equations (36) and (51) for $R_1 = 1$ and $R_2 = 0$, corresponding to a top heavy triangular profile. In (a) $\sigma_{\max}$ is plotted against the logarithm of L at times $T = 1$ (+), 10 (◯), 10^2 (∗), 10^3 (□), 10^4 (⋆), 10^5 (◇) and 10^6 (▽). The dotted line corresponds to equation (54). In (b) $\log_{10}(\sigma_{\max})$ is plotted against $\log_{10}(T)$ for thicknesses $L = 10$ (◯), 10^2 (∗), 10^3 (□) and 10^4 (⋆).

5.3 Decreasing gradients − Top heavy triangular profiles

In this subsection, we consider $R_1 = 1$ and $R_2 = 0$ so that we initially have a top heavy triangular profile. The profile for $\tilde{A}$ changes slowly near $X = 0$ where the gradient is initially most negative. A useful measure is to consider $\int_{-L/2}^{L/2} \tilde{A}\, dX$ which remains above 90% of the initial value of $L/2$ when $L \geq 11.284\sqrt{T}$.

In figure 14(a) the maximum instantaneous growth rate for the evolution of the piecewise linear profile (50) with $R_1 = 1$ and $R_2 = 0$, corresponding to a top heavy triangular profile, is plotted against the logarithm of L at various times. We observe that there is a most unstable thickness L for each time, in which reducing L or increasing L reduces the maximum instantaneous growth rate. Further, when L is very large, we see that the maximum instantaneous growth rate stays virtually constant for a very large time.

In appendix E we include the dispersion equation derived by Horton and Rogers [9] and Lapwood [10] for a fluid in a vertical region of height L with a constant density gradient of $(R_2 - R_1)/L$ with no flux boundary conditions, whose maximum growth rate is given by

$$\sigma_{\max} = \frac{R_1 - R_2}{L} - \frac{2\pi}{L^{3/2}}\sqrt{R_1 - R_2}. \tag{54}$$

Although our problem is in an infinite region, we observe that for large L and large T, the growth rates in figure 14(a) are very close to those predicted by equation (54) illustrated by a dotted line.

In figure 14(b) the logarithm of the maximum instantaneous growth rate for the evolution of the piecewise linear profile (50) with $R_1 = 1$ and $R_2 = 0$

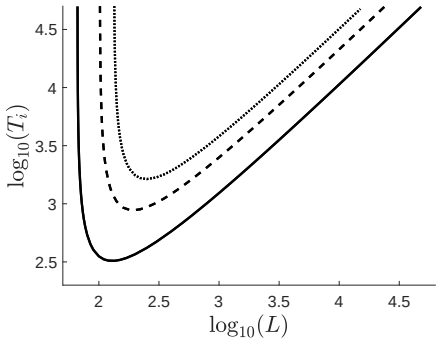

Fig. 15 Log-log plots relating T_i with L are presented for the initial piecewise linear profile (50) with thickness L for $R_1 = 1$ and $R_2 = 0$, corresponding to a top heavy triangular profile, obtained by numerically solving equations (36) and (51). The solid line corresponds to T_1, the dashed line to T_2 and the dotted line to T_3.

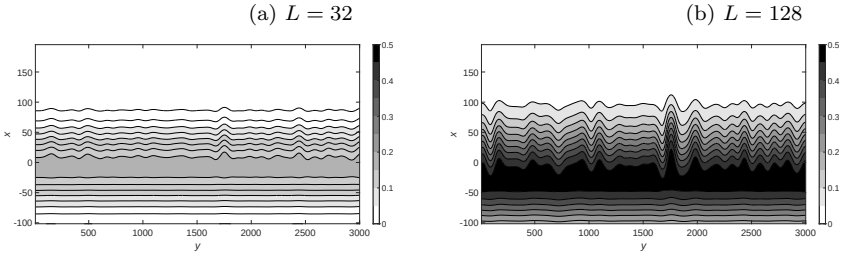

Fig. 16 Contours of A obtained from equations (14) and (15) with an initial condition corresponding to the piecewise linear profile (50) with $R_1 = 1$ and $R_2 = 0$, corresponding to a top heavy triangular profile, of thickness (a) $L = 32$ and (b) $L = 128$ at time $T = 10^3$.

is plotted against the logarithm of T for various thicknesses. We observe that the growth rates are virtually constant for a long period of time, and then decay like T^{-1}. Increasing the thickness L, increases the time delay for when the regime changes from a constant growth rate to a decaying growth rate.

When $R_1 = 1$ and $R_2 = 0$, in figure 15 we plot $\log_{10}(L)$ against $\log_{10}(T_i)$ for $i = 1$, 2 and 3. We observe that there appears to be a most unstable thickness L, as increasing or decreasing L yields a large value of T_i, however, this optimum value of L is different for T_1, T_2 and T_3. As before we observe that as L decreases towards a critical value, each T_i tends to infinity.

By performing numerical simulations we obtained the full solutions to equations (14) and (15) for an initial concentration profile corresponding to the piecewise linear profile (50) of thickness L for $R_1 = 1$ and $R_2 = 0$, corresponding to a top heavy triangular profile. Figure 16 shows contours of the concentration at time $T = 10^3$ for (a) $L = 32$ and (b) $L = 128$. Figure 16(b) for a thickness of $L = 128$ shows an instability which is significantly more pronounced than in figure 16(a) for a thickness of $L = 32$, as expected from the numerical linear stability analysis.

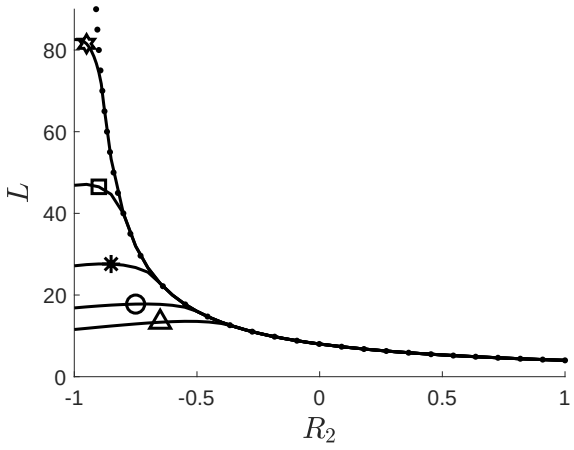

Fig. 17 Neutral stability curves for the initial piecewise linear profile (50) with thickness L with $R_1 = 1$, corresponding to a top heavy profile, obtained by numerically solving equations (36) and (51). Curves are illustrated at times $T = 0.001$ ($\triangle$), 10 ($\bigcirc$), 10^2 ($*$), 10^3 ($\square$) and 10^4 ($\star$). The dotted curve is the large time theoretical onset condition (52).

For $L = 128$ with $R_1 = 1$ and $R_2 = 0$, the numerical linear stability predicts that $T_1 = 332.49$ and $T_2 = 1257.9$. The fastest growing wavenumbers at these times are $k_{\max} = 0.0312$ and 0.0229, corresponding to wavelengths of 201.4 and 274.4 respectively. The full numerical simulation at time $T = 10^3$, shown in figure 16(b), has produced 17 fingers in a domain of thickness 3000. The average thickness of each finger is therefore around 176, which is consistent with the wavelengths predicted by the numerical linear stability analysis at time T_1.

5.4 Decreasing gradients − Top heavy profiles

In this subsection, we consider $R_1 = 1$ with $|R_2| \leq 1$, so that the density is greatest at $X = -L/2$, i.e. at the top of the layer. In figure 17 we present the neutral stability curves at various times when $R_1 = 1$, corresponding to a top heavy profile. The marginal stability curve in figure 17 resembles the marginal stability curve in figure 11 except the horizontal axis is now R_2 instead of R_1. Again, the neutral stability curve approaches the theoretically predicted condition (52) for large times.

When $R_1 = 1$ and $R_2 = -1$, in figure 18 we plot $\log_{10}(L)$ against $\log_{10}(T_i)$ for $i = 1$, 2 and 3. We observe that there appears to be a most unstable thickness L, as increasing or decreasing L yields a large value of T_i, however, this optimum value of L is different for each T_1, T_2 and T_3. For moderate values of L, the T_i curves turn back of themselves, showing that the product σT can decrease in time, so the system becomes less unstable in time. This result is

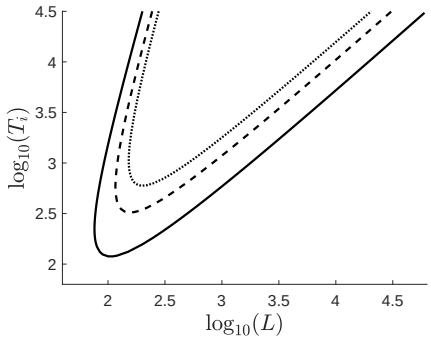

Fig. 18 Log-log plots relating T_i with L are presented for the initial piecewise linear profile (50) with thickness L for $R_1 = 1$ and $R_2 = -1$, corresponding to a top heavy profile, obtained by numerically solving equations (36) and (51). The solid line corresponds to T_1, the dashed line to T_2 and the dotted line to T_3.

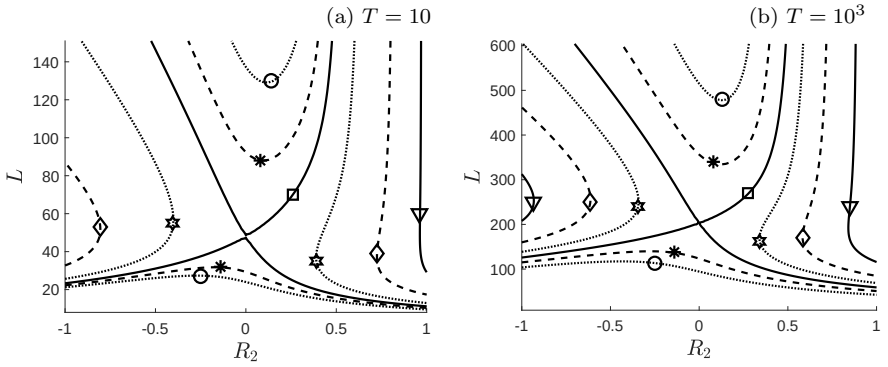

Fig. 19 Contours of the maximum instantaneous growth rate for the initial piecewise linear profile (50) for $R_1 = 1$, corresponding to a top heavy profile, obtained by numerically solving equations (36) and (51). In (a) $T = 10$ and contours are illustrated for $\sigma_{\max} = 0.004$ ($\bigcirc$), 0.005 ($*$), 0.006 ($\square$), 0.008 ($\star$), 0.012 ($\diamond$), 0.016 ($\triangledown$). In (b) $T = 10^3$ and contours are illustrated for $\sigma_{\max} = 0.0014$ ($\bigcirc$), 0.0018 ($*$), 0.002177 ($\square$), 0.0026 ($\star$), 0.0032 ($\diamond$), 0.004 ($\triangledown$).

expected, as the onset condition for an instability, equation (52), predicts that for large times the system will eventually be stable.

In figure 19 we present contours of the maximum instantaneous growth rate for the evolution of the piecewise linear profile (50) for $R_1 = 1$, corresponding to a top heavy profile, at times $T = 10$ and $T = 10^3$. Similar contours plots were found at other times but are not presented to avoid repetition. Although figure 19(a) at $T = 10$ resembles figure 19(b) at $T = 10^3$, we notice that the values of L are around 4 times larger. The growth rates are observed to be smallest for small L or for large L near $R_2 = 0$. The growth rates are largest near $R_2 = 1$, but also increase near $R_2 = -1$ for a narrow range of L, which

corresponds to an optimum thickness L. This optimum appears true for most values of R_2.

To summarise, numerically we have found that, for thick layers, the growth rates for the initial piecewise linear profile (50), when we have a top heavy profile, remain constant for a long time, however, later they decay like T^{-1}.

6 Conclusions

In this study we perform both linear stability analysis and full numerical simulations to examine buoyancy instabilities in a two dimensional vertically oriented porous medium. Using the quasi-steady state approximation, the linear stability analysis was reduced to an eigenvalue problem.

In section 3 we considered a species uniformly dissolved in the upper half of the domain, and absent from the bottom half of the domain. The numerical linear stability agreed well with the analytical solution obtained at time $T = 0$ by [23] for a related problem. Large time asymptotic analysis showed that the instantaneous growth rate decreases in time like $T^{-1/2}$, which were in agreement with the results obtained from the numerical linear stability analysis. Full numerical simulations produced density fingers with wavelengths in agreement with the predictions by the linear stability analysis.

In section 4 we considered a species initially uniformly distributed in a finite layer. The threshold condition for a long wave instability derived by [35] at time $T = 0$ was numerically found to hold for all time. Thin layers were found to have very weak instabilities, even when the layer was several times thicker than the threshold thickness for an instability to occur. For very thick layers, we found that for a long time the growth rates decayed like $T^{-1/2}$, but eventually decayed like T^{-1} with the time taken for them to start decaying like T^{-1} depending on L.

In section 5 we considered a species initially linearly distributed in a finite layer. When the concentration has an increasing gradient in the downwards direction, so that the density profiles were bottom heavy, the stability of the system was similar to that of a uniformly distributed finite layer, i.e. increasing the thickness or concentration of the species both has monotonic increasing affects on the stability of the system. For thick layers, the growth rates for the initially piecewise linear bottom heavy profile considered decayed with $T^{-1/2}$ (like a single step) for a long time, however, later they decay like T^{-1}. However, when the concentration had a decreasing gradient in the downwards direction, so that the density profiles were top heavy, the stability of the system behaved differently. For a thin layer the growth rates quickly decayed, however, for thick layers the growth rates remained constant for a long period time, but eventually decayed like T^{-1} for very large times. At a given time, the layer thickness had a non-monotonic affect on the stability of the system with thin and thick layers being less unstable than an optimum layer thickness, however, this optimum layer thickness increases in time.

Acknowledgements PMJT would like to thank Anne De Wit for fruitful discussions. Additionally the authors would like to thank the referees for their constructive comments which helped to improve the manuscript.

References

1. Lord Rayleigh (1883) Investigation of the character of the equilibrium of an incompressible heavy fluid of variable density. *Proc. Lond. Math. Soc.*, **14**: 170–177.
2. Taylor GI (1950) The instability of liquid surfaces when accelerated in a direction perpendicular to their planes. *Proc. R. Soc. Lond. A*, **201**: 192–196.
3. Cabot WH & Cook AW (2006) Reynolds number effects on Rayleigh-Taylor instability with possible implications for type-Ia supernovae. *Nature Physics*, **2**: 562–568.
4. Huang CS, Kelley MC & Hysell DL (1993) Nonlinear Rayleigh-Taylor instabilities,atmospheric gravity waves and equatorial spread F. *J. Geophys.Res.*, **98**: 15631–15642.
5. Gerya TV & Yuen DA (2003) Rayleigh-Taylor instabilities from hydration and melting propel 'cold plumes' at subduction zones. *Earth Planet. Sci. Lett.*, **212**: 47–62.
6. Conrad CP & Molnar P (1997) The growth of Rayleigh-Taylor-type instabilities in the lithosphere for various rheological and density structures. *Geophy. J. Int.*, **129**: 95–112.
7. Sharp DH (1984) An overview of Rayleigh-Taylor instability. *Physica D*, **12**: 3–18.
8. Citri O, Kagan ML, Kosloff R & Avnir D (1990) The evolution of chemically induced unstable density gradients near horizontal reactive interfaces. *Langmuir*, **6**: 559–564.
9. Horton CW & Rogers Jr. FT (1945) Convection currents in porous media. *J. Appl. Phys.*, **20**: 367–369.
10. Lapwood ER (1948) Convection of a fluid in a porous medium. *Proc. Cambridge Phil. Soc.*, **44**: 508–521.
11. Stommel H, Arons AB & Blanchard D (1956) An oceanographic curiosity: the perpetual salt fountain. *Deep-Sea Res.*, **3**: 152–152.
12. Stern ME (1960) The salt-fountain and thermohaline convection. *Tellus*, **12**: 172–177.
13. Huppert HE & Mannis PC (1973) Limiting conditions for salt-fingering at an interface. *Deep Sea Res.*, **20**: 315–323.
14. Trevelyan PMJ, Almarcha C & De Wit A (2011) Buoyancy-driven instabilities of miscible two-layer stratifications in porous media and Hele-Shaw cells. *J. Fluid Mech.*, **670**: 38–65.
15. Saffman PG & Taylor G (1958) The penetration of a fluid into a medium or Hele-Shaw cell containing a more viscous liquid. *Proc. Soc. London, Ser A.*, **245**: 312–329.
16. Homsy GM (1987) Viscous fingering in porous media. *Ann. Rev. Fluid Mech.*, **19**: 271–311.
17. Pritchard D (2009) The linear stability of double-diffusive miscible rectilinear displacements in a Hele-Shaw cell. *Euro. J. Mech. B. Fluids*, **28**: 564–577.
18. Mishra M, Trevelyan PMJ, Almarcha C & De Wit A (2010) Influence of double diffusive effects on miscible viscous fingering. *Phys. Rev. Lett.*, **105**: 204501.
19. De Wit A (2016) Chemo-hydrodynamic patterns in porous media. *Phil. Trans. R. Soc. A*, **374**: 20150419.
20. Hickernell FJ & Yortsos YC (1986) Linear stability of miscible displacement processes in porous media in the absence of dispersion. *Stud. Appl. Math.*, **74**: 93–115.
21. Manickam O & Homsy GM (1993) Stability of miscible displacements in porous media with non-monotonic viscosity profiles. *Phys. Fluids A*, **5**: 1356–1367.
22. Manickam O & Homsy GM (1994) Simulation of viscous fingering in miscible displacements with non-monotonic viscosity profiles. *Phys. Fluids*, **9**: 95–107.
23. Tan CT & Homsy GM (1986) Stability of miscible displacements in porous media: rectilinear flow. *Phys. Fluids*, **29**: 3549–3556.
24. Ben Y, Demekhin EA & Chang HC (2002) A spectral theory for small amplitude miscible fingering. *Phys. Fluids*, **14**: 999–1010.
25. Kim MC (2012) Linear stability analysis on the onset of the viscous fingering of a slice in a porous medium. *Adv. Water Res.*, **35**: 1–9.

26. Hota TK, Pramanik S & Mishra M (2015) Onset of fingering instability in a finite slice of adsorbed solute. *Phys. Rev. E*, **92**: 023013.
27. Trevelyan PMJ, Almarcha C & De Wit A (2015) Buoyancy-driven instabilities around $A + B \to C$ reaction fronts: A general classification. *Phys. Rev. E*, **91**: 023001.
28. Kim MC (2014) Effect of the irreversible $A + B \to C$ reaction on the onset and the growth of the buoyancy-driven instability in a porous medium. *Chem. Eng. Sci.*, **112**: 56–71.
29. Kim MC (2019) Effect of the irreversible $A + B \to C$ reaction on the onset and the growth of the buoyancy-driven instability in a porous medium: Asymptotic, linear, and nonlinear stability analyses. *Phys. Rev. Fluids*, **4**: 073901.
30. Hejazi SH, Trevelyan PMJ, Azaiez J & De Wit A (2010) Viscous fingering of a miscible reactive $A + B \to C$ interface: A linear stability analysis. *J. Fluid Mech.*, **652**: 501–528.
31. Riaz A, Hesse M, Tchelepi HA & Orr FM (2006) Onset of convection in a gravitationally unstable diffusive boundary layer in porous media. *J. Fluid Mech.*, **548**: 87–111.
32. Kim MC (2015) Linear and nonlinear analyses on the onset of gravitational instabilities in a fluid saturated with in a vertical Hele-Shaw cell. *Chem. Eng. Sci.*, **126**: 349–360.
33. Kim MC & Song KH (2017) Effect of impurities on the onset and growth of gravitational instabilities in a geological CO_2 storage process: Linear and nonlinear analyses. *Chem. Eng. Sci.*, **174**: 426–444.
34. Kim MC & Wylock C (2017) Linear and nonlinear analyses of the effect of chemical reaction on the onset of buoyancy-driven instability in a CO_2 absorption process in a porous medium or Hele-Shaw cell. *Canadian J. Chem. Eng.*, **96**: 105–118.
35. Gandhi J & Trevelyan PMJ (2014) Onset conditions for a Rayleigh-Taylor instability with step function density profiles. *J. Eng. Math.*, **86**: 31–48.
36. Kim MC (2015) Linear stability analysis on the onset of the Rayleigh-Taylor instability of a miscible slice in a porous medium. *J. Eng. Math.*, **90**: 105–118.
37. Nield DA & Bejan A (2006) Convection in porous media. *New York, Springer*.
38. Martin J, Rakotomalala N & Salin D (2002) Gravitational instability of miscible fluids in a Hele-Shaw cell. *Phys. Fluids*, **14**: 902–905.
39. Fulton SR, Ciesielski PE & Schubert WH (1986) Multigrid methods for elliptic problems: a review. *Mon. Weather Rev.*, **114**: 943–959.
40. Lin S-J & Rood RB (1996) Multidimensional flux-form semi-Lagrangian transport schemes. *Mon. Weather Rev.*, **124**: 2046–2070.
41. Holdaway D & Kent J (2015) Assessing the tangent linear behaviour of common tracer transport schemes and their use in a linearised atmospheric general circulation model. *Tellus A*, **67**: 27895.
42. Kalliadasis S, Yang J & De Wit A (2004) Fingering instabilities of exothermic reaction-diffusion fronts in porous media. *Phys. Fluids*, **16**: 1395–1409.

A Mesh

For the numerical linear stability analysis we use a non-uniform mesh. We choose the number of spatial nodes n to be of the form $n = 4m + 1$. The whole domain is $X \in [-W, W]$. We choose to uniformly distribute around half of the nodes inside $X \in [-L/2, L/2]$. Outside of this central region we distribute the nodes so that the distance between them are in a geometric progression. Hence, we locate the nodes at:

$$X_i = \begin{cases} -\dfrac{L}{2} - \dfrac{L}{2m}\left(\dfrac{\theta^{m+1-i}-1}{\theta-1}\right) & \text{for} \quad 1 \leq \ i \ \leq m+1 \\ \dfrac{L}{2m}(i-2m-1) & \text{for} \quad m+1 \leq \ i \ \leq 3m+1 \\ \dfrac{L}{2} + \dfrac{L}{2m}\left(\dfrac{\theta^{i-3m-1}-1}{\theta-1}\right) & \text{for} \quad 3m+1 \leq \ i \ \leq 4m+1. \end{cases} \tag{55}$$

This form has been chosen so that the nodes pass through the points $X_{m+1} = -L/2$, $X_{2m+1} = 0$ and $X_{3m+1} = L/2$, and further, so that the distance between the nodes are

equal where the uniform and non-uniform mesh meet, i.e. $X_{m+1} - X_m = X_{m+2} - X_{m+1} = X_{3m+1} - X_{3m} = X_{3m+2} - X_{3m+1} = L/(2m)$. Finally, in order for the nodes to satisfy $X_1 = -W$ and $X_n = W$ we require that θ satisfies

$$\theta^m - m\left(\frac{2W}{L} - 1\right)(\theta - 1) - 1 = 0. \tag{56}$$

Once, L, W and m have been given values, this equation was numerically solved for θ using an initial guess of $\theta = 1.1$ with the Newton-Raphson method.

B Finite differences

We approximate the second derivative using a five point third order accurate finite difference scheme of the form

$$\Phi_{XX}|_{X_i} = a_i\Phi_{i-2} + b_i\Phi_{i-1} + c_i\Phi_i + d_i\Phi_{i+1} + e_i\Phi_{i+2} \tag{57}$$

where $\Phi_i = \Phi(X_i)$ and the constants a_i, b_i, c_i, d_i and e_i are given by

$$\begin{aligned}
a_i &= \frac{2(3X_i^2 - 2X_iX_{i+1} - 2X_iX_{i+2} - 2X_iX_{i-1} + X_{i+1}X_{i+2} + X_{i+1}X_{i-1} + X_{i+2}X_{i-1})}{(X_{i+2} - X_{i-2})(X_{i+1} - X_{i-2})(X_i - X_{i-2})(X_{i-1} - X_{i-2})} \\
b_i &= \frac{2(3X_i^2 - 2X_iX_{i+1} - 2X_iX_{i+2} - 2X_iX_{i-2} + X_{i+1}X_{i+2} + X_{i+1}X_{i-2} + X_{i+2}X_{i-2})}{(X_{i+2} - X_{i-1})(X_{i+1} - X_{i-1})(X_i - X_{i-1})(X_{i-2} - X_{i-1})} \\
c_i &= \frac{2(6X_i^2 - 3X_iX_{i+1} - 3X_iX_{i+2} - 3X_iX_{i-1} - 3X_iX_{i-2} + X_{i+1}X_{i+2})}{(X_{i+2} - X_i)(X_{i+1} - X_i)(X_{i-1} - X_i)(X_{i-2} - X_i)} \\
&\quad + \frac{2(X_{i+1}X_{i-1} + X_{i+1}X_{i-2} + X_{i+2}X_{i-1} + X_{i+2}X_{i-2} + X_{i-1}X_{i-2})}{(X_{i+2} - X_i)(X_{i+1} - X_i)(X_{i-1} - X_i)(X_{i-2} - X_i)} \\
d_i &= \frac{2(3X_i^2 - 2X_iX_{i+2} - 2X_iX_{i-1} - 2X_iX_{i-2} + X_{i-1}X_{i-2} + X_{i+2}X_{i-1} + X_{i+2}X_{i-2})}{(X_{i+2} - X_{i+1})(X_i - X_{i+1})(X_{i-1} - X_{i+1})(X_{i-2} - X_{i+1})} \\
e_i &= \frac{2(3X_i^2 - 2X_iX_{i-1} - 2X_iX_{i-2} - 2X_iX_{i+1} + X_{i-1}X_{i-2} + X_{i-1}X_{i+1} + X_{i-2}X_{i+1})}{(X_{i+1} - X_{i+2})(X_i - X_{i+2})(X_{i-1} - X_{i+2})(X_{i-2} - X_{i+2})}
\end{aligned}$$

for $3 \le i \le n-2$. Near the left hand boundary we use the no flux boundary condition within the approximation for the second derivative using a four point third order accurate finite difference scheme of the form

$$\Phi_{XX}|_{X_1} = c_1\Phi_1 + d_1\Phi_2 + e_1\Phi_3 + f_1\Phi_4 \tag{58}$$

$$\Phi_{XX}|_{X_2} = b_2\Phi_1 + c_2\Phi_2 + d_2\Phi_3 + e_2\Phi_4 \tag{59}$$

where

$$\begin{aligned}
c_1 &= -2\frac{(X_3 - X_1)^2 + (X_3 - X_1)(X_4 - X_1) + (X_4 - X_1)^2}{(X_3 - X_1)^2(X_4 - X_1)^2} \\
&\quad - 2\frac{(X_2 - X_1)(X_3 - X_1) + (X_2 - X_1)(X_4 - X_1) + (X_3 - X_1)(X_4 - X_1)}{(X_2 - X_1)^2(X_3 - X_1)(X_4 - X_1)} \\
d_1 &= \frac{2(X_3 - X_1)(X_4 - X_1)}{(X_1 - X_2)^2(X_3 - X_2)(X_4 - X_2)} \\
e_1 &= \frac{2(X_2 - X_1)(X_4 - X_1)}{(X_1 - X_3)^2(X_2 - X_3)(X_4 - X_3)} \\
f_1 &= \frac{2(X_2 - X_1)(X_3 - X_1)}{(X_1 - X_4)^2(X_2 - X_4)(X_3 - X_4)}
\end{aligned}$$

and

$$
\begin{aligned}
b_2 &= \frac{2(X_3 - X_2)(X_4 - X_2)}{(X_2 - X_1)^2(X_3 - X_1)(X_4 - X_1)} \\
c_2 &= -2\frac{3X_2^2 - 3X_2X_1 - 3X_2X_4 + X_1^2 + X_1X_4 + X_4^2}{(X_1 - X_2)^2(X_4 - X_2)^2} \\
&\quad - 2\frac{3X_2^2 - 2X_2X_1 - 2X_2X_3 - 2X_2X_4 + X_1X_3 + X_1X_4 + X_3X_4}{(X_1 - X_2)(X_3 - X_2)^2(X_4 - X_2)} \\
d_2 &= \frac{2(X_1 - X_2)(X_4 - X_2)}{(X_1 - X_3)(X_2 - X_3)^2(X_4 - X_3)} \\
e_2 &= \frac{2(X_1 - X_2)(X_3 - X_2)}{(X_1 - X_4)(X_2 - X_4)^2(X_3 - X_4)}.
\end{aligned}
$$

Similarly, near the right hand boundary we use the no flux boundary condition within the approximation for the second derivative using a four point third order accurate finite difference scheme of the form

$$\Phi_{XX}|_{X_{n-1}} = a_{n-1}\Phi_{n-3} + b_{n-1}\Phi_{n-2} + c_{n-1}\Phi_{n-1} + d_{n-1}\Phi_n \tag{60}$$

$$\Phi_{XX}|_{X_n} = f_n\Phi_{n-3} + a_n\Phi_{n-2} + b_n\Phi_{n-1} + c_n\Phi_n \tag{61}$$

where

$$
\begin{aligned}
a_{n-1} &= \frac{2(X_n - X_{n-1})(X_{n-2} - X_{n-1})}{(X_n - X_{n-3})(X_{n-1} - X_{n-3})^2(X_{n-2} - X_{n-3})} \\
b_{n-1} &= \frac{2(X_n - X_{n-1})(X_{n-3} - X_{n-1})}{(X_n - X_{n-2})(X_{n-1} - X_{n-2})^2(X_{n-3} - X_{n-2})} \\
c_{n-1} &= -2\frac{3X_{n-1}^2 - 3X_{n-1}X_{n-3} - 3X_{n-1}X_{n-2} + X_{n-3}^2 + X_{n-3}X_{n-2} + X_{n-2}^2}{(X_{n-2} - X_{n-1})^2(X_{n-3} - X_{n-1})^2} \\
&\quad - 2\frac{3X_{n-1}^2 - 2X_{n-1}X_{n-3} - 2X_{n-1}X_{n-2} - 2X_{n-1}X_n + X_{n-3}X_{n-2} + X_{n-3}X_n + X_{n-2}X_n}{(X_n - X_{n-1})^2(X_{n-2} - X_{n-1})(X_{n-3} - X_{n-1})} \\
d_{n-1} &= \frac{2(X_{n-2} - X_{n-1})(X_{n-3} - X_{n-1})}{(X_{n-1} - X_n)^2(X_{n-2} - X_n)(X_{n-3} - X_n)}
\end{aligned}
$$

and

$$
\begin{aligned}
f_n &= \frac{2(X_{n-1} - X_n)(X_{n-2} - X_n)}{(X_n - X_{n-3})^2(X_{n-1} - X_{n-3})(X_{n-2} - X_{n-3})} \\
a_n &= \frac{2(X_{n-1} - X_n)(X_{n-3} - X_n)}{(X_n - X_{n-2})^2(X_{n-1} - X_{n-2})(X_{n-3} - X_{n-2})} \\
b_n &= \frac{2(X_{n-2} - X_n)(X_{n-3} - X_n)}{(X_n - X_{n-1})^2(X_{n-2} - X_{n-1})(X_{n-3} - X_{n-1})} \\
c_n &= -2\frac{(X_n - X_{n-2})^2 + (X_n - X_{n-2})(X_n - X_{n-3}) + (X_n - X_{n-3})^2}{(X_{n-2} - X_n)^2(X_{n-3} - X_n)^2} \\
&\quad - 2\frac{(X_n - X_{n-1})(X_n - X_{n-2}) + (X_n - X_{n-1})(X_n - X_{n-3}) + (X_n - X_{n-2})(X_n - X_{n-3})}{(X_{n-1} - X_n)^2(X_{n-2} - X_n)(X_{n-3} - X_n)}.
\end{aligned}
$$

Putting all this together, we can construct the matrix

$$\underline{\underline{S}} = \begin{bmatrix} c_1 & d_1 & e_1 & f_1 & 0 & 0 & \cdots & 0 & 0 & 0 & 0 & 0 & 0 \\ b_2 & c_2 & d_2 & e_2 & 0 & 0 & \cdots & 0 & 0 & 0 & 0 & 0 & 0 \\ a_3 & b_3 & c_3 & d_3 & e_3 & 0 & \cdots & 0 & 0 & 0 & 0 & 0 & 0 \\ 0 & a_4 & b_4 & c_4 & d_4 & e_4 & \cdots & 0 & 0 & 0 & 0 & 0 & 0 \\ 0 & 0 & a_5 & b_5 & c_5 & d_5 & \cdots & 0 & 0 & 0 & 0 & 0 & 0 \\ 0 & 0 & 0 & a_6 & b_6 & c_6 & \cdots & 0 & 0 & 0 & 0 & 0 & 0 \\ \vdots & \vdots & \vdots & \vdots & \vdots & \vdots & \ddots & \vdots & \vdots & \vdots & \vdots & \vdots & \vdots \\ 0 & 0 & 0 & 0 & 0 & 0 & \cdots & c_{n-5} & d_{n-5} & e_{n-5} & 0 & 0 & 0 \\ 0 & 0 & 0 & 0 & 0 & 0 & \cdots & b_{n-4} & c_{n-4} & d_{n-4} & e_{n-4} & 0 & 0 \\ 0 & 0 & 0 & 0 & 0 & 0 & \cdots & a_{n-3} & b_{n-3} & c_{n-3} & d_{n-3} & e_{n-3} & 0 \\ 0 & 0 & 0 & 0 & 0 & 0 & \cdots & 0 & a_{n-2} & b_{n-2} & c_{n-2} & d_{n-2} & e_{n-2} \\ 0 & 0 & 0 & 0 & 0 & 0 & \cdots & 0 & 0 & a_{n-1} & b_{n-1} & c_{n-1} & d_{n-1} \\ 0 & 0 & 0 & 0 & 0 & 0 & \cdots & 0 & 0 & f_n & a_n & b_n & c_n \end{bmatrix}. \tag{62}$$

C Large time asymptotic analysis for a step

By substituting equation (40), corresponding to the evolution of an initial step function profile, into the system of equations (25) and (26) and then by making the rescalings $X = x_0 z$ and $k = \kappa/x_0$ we obtain

$$\mathcal{F}_{zz} = \kappa^2(\mathcal{A} + \mathcal{F}) \quad \text{and} \quad \sigma\mathcal{A} = \frac{\mathcal{A}_{zz}}{x_0^2} - \frac{\kappa^2}{x_0^2}\mathcal{A} - \frac{\mathcal{F}}{\sqrt{4\pi T}} \exp\left(-\frac{z^2 x_0^2}{4T}\right). \tag{63}$$

Then we assume that $x_0 \ll \sqrt{T}$ so that the exponential function can be approximated by unity. (We note that numerically we find that $k_{\max} = O(T^{-1/3})$ so that $x_0 = T^{1/3}$, which satisfies $x_0 \ll \sqrt{T}$). Next, we assume that spatial gradients tend to zero everywhere as T tends to infinity. The first equation gives $\mathcal{A} = -\mathcal{F}$ which when substituted into the second equation yields

$$\sigma = \frac{1}{\sqrt{4\pi T}} - \frac{\kappa^2}{x_0^2}. \tag{64}$$

First we consider the maximum instantaneous growth rate, in the large time limit, with the assumption that $x_0 \ll \sqrt{T}$, equation (64) yields

$$\sigma\text{max} \approx \frac{1}{\sqrt{4\pi T}}. \tag{65}$$

Second we consider the cut off wavenumber, i.e. when $\sigma = 0$, and now equation (64) yields

$$\frac{\kappa_{\text{cut}}^2}{x_0^2} = \frac{1}{\sqrt{4\pi T}}. \tag{66}$$

For this to be consistent in the large time limit we require that $x_0 = T^{1/4}$, then we have shown that

$$\kappa_{\text{cut}} = \frac{1}{(4\pi)^{1/4}} \quad \Longrightarrow \quad k_{\text{cut}} \approx \frac{1}{(4\pi T)^{1/4}}. \tag{67}$$

D Linear stability for the piecewise linear profile (50)

Here we derive the dispersion equation at time $T = 0$ for a base state concentration profile in the form of a piecewise linear profile with concentration R_1 at $X = -L/2$ and R_2 at $X = L/2$, and zero everywhere else, i.e. equation (50), namely

$$\tilde{A}(X,0) = \frac{1}{2L}\left[R_1\left(L-2X\right) + R_2\left(L+2X\right)\right] H(L^2 - 4X^2).$$

The eigenfunctions $\mathcal{A}$ and $\mathcal{F}$ need to satisfy equation (25) and (26) namely

$$\begin{aligned} \mathcal{F}_{XX} &= k^2(\mathcal{A}+\mathcal{F}), \\ \sigma\mathcal{A} &= \mathcal{A}_{XX} - k^2\mathcal{A} + \mathcal{F}\tilde{A}_X \end{aligned}$$

subject to the far field conditions equation (27) namely

$$\mathcal{A}_X \to 0 \quad \text{and} \quad \mathcal{F}_X \to 0 \quad \text{as} \quad X \to \pm\infty.$$

As the coefficients in the ordinary differential equations are all constants, we can seek a solution of the form

$$[\mathcal{A}, \mathcal{F}] = [c_A, c_F]e^{\lambda X} \tag{68}$$

where c_A and c_F are constants. Substituting these expressions into the ODEs yields

$$\lambda^2 c_F = k^2(c_A + c_F) \quad \text{and} \quad \sigma c_A = \lambda^2 c_A - k^2 c_A + c_F\tilde{A}_X. \tag{69}$$

The first equation yields $c_F = k^2 c_A/(\lambda^2 - k^2)$ and substituting this into the second equation gives

$$(\lambda^2 - \sigma - k^2)(\lambda^2 - k^2) + k^2\tilde{A}_X = 0. \tag{70}$$

For $|2X| > L$, then $\tilde{A}_X = 0$ and we obtain $\lambda = \pm k$ and $\lambda = \pm\sqrt{\sigma + k^2}$, but for $|2X| < L$, then $\tilde{A}_X \neq 0$ and so we have the quartic

$$\lambda^4 - (2k^2 + \sigma)\lambda^2 + k^4 + (\sigma + r)k^2 = 0 \tag{71}$$

where $r = (R_2 - R_1)/L$, i.e. $r = \tilde{A}_X$ for $|2X| < L$. Solving this quartic yields

$$\lambda^2 = k^2 + \frac{\sigma \pm q}{2} \quad \text{where} \quad q^2 = \sigma^2 - 4rk^2. \tag{72}$$

Using these values of λ along with the far field boundary conditions we obtain

$$\mathcal{F} = \begin{cases} \mathcal{F}^T = F_1 k^2 e^{k(2X+L)/2} + F_2 k^2 e^{\lambda_1(2X+L)/2}, & \text{for} \quad X < -L/2, \\ \mathcal{F}^M = k^2(F_3 e^{\lambda_2 X} + F_4 e^{-\lambda_2 X} + F_5 e^{\lambda_3 X} + F_6 e^{-\lambda_3 X}), & \text{for} \quad |X| < L/2, \\ \mathcal{F}^B = F_7 k^2 e^{-k(2X-L)/2} + F_8 k^2 e^{-\lambda_1(2X-L)/2}, & \text{for} \quad X > L/2 \end{cases} \tag{73}$$

and

$$\mathcal{A} = \begin{cases} \mathcal{A}^T = \sigma F_2 e^{\lambda_1(2X+L)/2}, & \text{for} \quad X < -L/2, \\ \mathcal{A}^M = \begin{array}{l} \frac{1}{2}(\sigma+q)(F_3 e^{\lambda_2 X} + F_4 e^{-\lambda_2 X}) \\ +\frac{1}{2}(\sigma-q)(F_5 e^{\lambda_3 X} + F_6 e^{-\lambda_3 X}) \end{array}, & \text{for} \quad |X| < L/2, \\ \mathcal{A}^B = \sigma F_8 e^{-\lambda_1(2X-L)/2}, & \text{for} \quad X > L/2 \end{cases} \tag{74}$$

where F_j for $j = 1$ to 8 are constants and

$$\lambda_1^2 = k^2 + \sigma, \quad \lambda_2^2 = k^2 + \frac{\sigma+q}{2}, \quad \text{and} \quad \lambda_3^2 = k^2 + \frac{\sigma-q}{2}. \tag{75}$$

Now we require that the eigenfunctions are continuous, hence, we need

$$\mathcal{A}^T = \mathcal{A}^M, \text{ and } \mathcal{F}^T = \mathcal{F}^M \quad \text{at} \quad X = -L/2, \tag{76}$$

$$\mathcal{A}^M = \mathcal{A}^B, \text{ and } \mathcal{F}^M = \mathcal{F}^B \quad \text{at} \quad X = L/2. \tag{77}$$

Using these 4 conditions we can eliminate the constants F_1, F_2, F_7 and F_8 so that the solutions $\mathcal{A}^T$, $\mathcal{F}^T$, $\mathcal{A}^B$ and $\mathcal{F}^B$ become

$$\begin{aligned}
\mathcal{A}^T &= \frac{1}{2}(\sigma+q)(F_3e^{-\lambda_2 L/2}+F_4e^{\lambda_2 L/2})e^{\lambda_1(2X+L)/2} \\
&\quad + \frac{1}{2}(\sigma-q)(F_5e^{-\lambda_3 L/2}+F_6e^{\lambda_3 L/2})e^{\lambda_1(2X+L)/2}, \qquad (78)\\
\mathcal{F}^T &= \frac{k^2}{2\sigma}(F_3e^{-\lambda_2 L/2}+F_4e^{\lambda_2 L/2})\left((\sigma-q)e^{k(2X+L)/2}+(\sigma+q)e^{\lambda_1(2X+L)/2}\right) \\
&\quad + \frac{k^2}{2\sigma}(F_5e^{-\lambda_3 L/2}+F_6e^{\lambda_3 L/2})\left((\sigma+q)e^{k(2X+L)/2}+(\sigma-q)e^{\lambda_1(2X+L)/2}\right), \qquad (79)\\
\mathcal{A}^B &= \frac{1}{2}(\sigma+q)(F_3e^{\lambda_2 L/2}+F_4e^{-\lambda_2 L/2})e^{-\lambda_1(2X-L)/2} \\
&\quad + \frac{1}{2}(\sigma-q)(F_5e^{\lambda_3 L/2}+F_6e^{-\lambda_3 L/2})e^{-\lambda_1(2X-L)/2}, \qquad (80)\\
\mathcal{F}^B &= \frac{k^2}{2\sigma}(F_3e^{\lambda_2 L/2}+F_4e^{-\lambda_2 L/2})\left((\sigma-q)e^{-k(2X-L)/2}+(\sigma+q)e^{-\lambda_1(2X-L)/2}\right) \\
&\quad + \frac{k^2}{2\sigma}(F_5e^{\lambda_3 L/2}+F_6e^{-\lambda_3 L/2})\left((\sigma+q)e^{-k(2X-L)/2}+(\sigma-q)e^{-\lambda_1(2X-L)/2}\right). \qquad (81)
\end{aligned}$$

By integrating the ODEs over the intervals $[-\frac{L}{2}-\epsilon,-\frac{L}{2}+\epsilon]$ and $[\frac{L}{2}-\epsilon,\frac{L}{2}+\epsilon]$ and letting $\epsilon\to 0$ we can evaluate the integrals using the jumps in $\tilde{A}$, as $\tilde{A}_X$ is a multiple of the Dirac delta function, to give

$$\mathcal{F}^M_X=\mathcal{F}^T_X \quad\text{and}\quad \mathcal{A}^T_X-\mathcal{A}^M_X=R_1\mathcal{F}^T \quad \text{at } X=-L/2 \qquad (82)$$
$$\mathcal{F}^B_X=\mathcal{F}^M_X \quad\text{and}\quad \mathcal{A}^B_X-\mathcal{A}^M_X=R_2\mathcal{F}^B \quad \text{at } X=L/2. \qquad (83)$$

These yield the 4 conditions

$$\begin{aligned}
0 &= P_1F_3-P_2F_4+P_3F_5-P_4F_6, \qquad (84)\\
0 &= P_2F_3-P_1F_4+P_4F_5-P_3F_6, \qquad (85)\\
0 &= Q_1F_3+Q_2F_4+Q_3F_5+Q_4F_6, \qquad (86)\\
0 &= S_1F_3+S_2F_4+S_3F_5+S_4F_6 \qquad (87)
\end{aligned}$$

where

$$\begin{aligned}
P_1 &= e^{-\lambda_2 L/2}(2\lambda_2\sigma-(\sigma-q)k-(\sigma+q)\lambda_1),\\
P_2 &= e^{\lambda_2 L/2}(2\lambda_2\sigma+(\sigma-q)k+(\sigma+q)\lambda_1),\\
P_3 &= e^{-\lambda_3 L/2}(2\lambda_3\sigma-(\sigma+q)k-(\sigma-q)\lambda_1),\\
P_4 &= e^{\lambda_3 L/2}(2\lambda_3\sigma+(\sigma+q)k+(\sigma-q)\lambda_1),\\
Q_1 &= e^{-\lambda_2 L/2}((\sigma+q)(\lambda_1-\lambda_2)-2R_1k^2),\\
Q_2 &= e^{\lambda_2 L/2}((\sigma+q)(\lambda_1+\lambda_2)-2R_1k^2),\\
Q_3 &= e^{-\lambda_3 L/2}((\sigma-q)(\lambda_1-\lambda_3)-2R_1k^2),\\
Q_4 &= e^{\lambda_3 L/2}((\sigma-q)(\lambda_1+\lambda_3)-2R_1k^2),\\
S_1 &= e^{\lambda_2 L/2}((\sigma+q)(\lambda_1+\lambda_2)+2R_2k^2),\\
S_2 &= e^{-\lambda_2 L/2}((\sigma+q)(\lambda_1-\lambda_2)+2R_2k^2),\\
S_3 &= e^{\lambda_3 L/2}((\sigma-q)(\lambda_1+\lambda_3)+2R_2k^2),\\
S_4 &= e^{-\lambda_3 L/2}((\sigma-q)(\lambda_1-\lambda_3)+2R_2k^2).
\end{aligned}$$

For this homogeneous linear system of equations to have a non-trivial solution for F_3, F_4, F_5 and F_6, we require that the coefficient matrix has a determinant of zero, i.e.

$$0 = \begin{vmatrix} P_1 & -P_2 & P_3 & -P_4 \\ P_2 & -P_1 & P_4 & -P_3 \\ Q_1 & Q_2 & Q_3 & Q_4 \\ S_1 & S_2 & S_3 & S_4 \end{vmatrix} \tag{88}$$

and thus we obtain the dispersion equation

$$\begin{aligned} 0 = {} & (Q_3S_4 - Q_4S_3)(P_2^2 - P_1^2) + (Q_2S_1 - Q_1S_2)(P_3^2 - P_4^2) \\ & + (P_1P_3 - P_2P_4)(Q_1S_4 - Q_4S_1 + S_2Q_3 - Q_2S_3) \\ & + (P_1P_4 - P_3P_2)(Q_1S_3 - Q_3S_1 + S_2Q_4 - Q_2S_4). \end{aligned} \tag{89}$$

E Linear stability for a linear profile

Suppose we have a linear concentration profile with a gradient of $(R_2 - R_1)/L$, given by

$$\tilde{A}(X, 0) = \frac{R_1 + R_2}{2} + \frac{(R_2 - R_1)X}{L}. \tag{90}$$

The eigenfunctions $\mathcal{A}$ and $\mathcal{F}$ need to satisfy equation (25) and (26) namely

$$\mathcal{F}_{XX} = k^2(\mathcal{A} + \mathcal{F}), \tag{91}$$

$$\sigma\mathcal{A} = \mathcal{A}_{XX} - k^2\mathcal{A} + \frac{(R_2 - R_1)}{L}\mathcal{F}. \tag{92}$$

If we have a finite domain of thickness L with no flux boundary conditions, namely

$$\mathcal{A}_X = \mathcal{F}_X = 0 \quad \text{at} \quad X = \pm\frac{L}{2} \tag{93}$$

then using $\mathcal{A} = c_A \sin\left(\frac{\pi X}{L}\right)$ and $\mathcal{F} = c_F \sin\left(\frac{\pi X}{L}\right)$ we obtain the dispersion equation

$$\sigma = \frac{(R_1 - R_2)Lk^2}{\pi^2 + L^2k^2} - k^2 - \frac{\pi^2}{L^2} \tag{94}$$

which means that

$$k^2_{\max} = \frac{\pi\sqrt{R_1 - R_2}}{L^{3/2}} - \frac{\pi^2}{L^2} \quad \text{and} \quad \sigma_{\max} = \frac{R_1 - R_2}{L} - \frac{2\pi\sqrt{R_1 - R_2}}{L^{3/2}} \tag{95}$$

and has an onset condition of

$$L(R_1 - R_2) > 4\pi^2. \tag{96}$$